

---

# Stochastic Attention via Langevin Dynamics on the Modern Hopfield Energy\*

---

Abdulrahman Alswaidan and Jeffrey D. Varner

R.F. Smith School of Chemical and Biomolecular Engineering  
Cornell University, Ithaca, NY 14850  
{aa2725, jdv27}@cornell.edu

## Abstract

Attention heads retrieve: given a query, they return a softmax-weighted average of stored values. We show that this computation is one step of gradient descent on a classical energy function, and that Langevin sampling from the corresponding distribution yields *stochastic attention*: a training-free sampler controlled by a single temperature. Lowering the temperature gives exact retrieval; raising it gives open-ended generation. Because the energy gradient equals the attention map, no score network, training loop, or learned model is required. We derive a closed-form entropy inflection condition that identifies the retrieval-to-generation transition temperature for any memory geometry, with a scaling law  $\beta^* \sim \sqrt{d}$  for random patterns. We validate on five domains (64 to 4,096 dimensions). On MNIST digit images, stochastic attention is  $2.6\times$  more novel and  $2.0\times$  more diverse than the best learned baseline (a VAE trained on the same patterns), while matching a Metropolis-corrected gold standard. On protein sequences from the Pfam RRM family, the generation regime achieves  $6.9\times$  lower amino acid composition divergence than the VAE (KL = 0.060 vs. 0.416) at matched novelty, demonstrating that the training-free score function preserves family-level fidelity that learned models lose. A denoising diffusion baseline (DDPM) fails across all memory sizes tested ( $K = 100$  to 3,500), producing samples indistinguishable from isotropic noise. The approach requires no architectural changes to the underlying attention mechanism.

## 1 Introduction

Attention is the central computational primitive of modern deep learning [1]. Given a query, it computes a softmax-weighted average of stored values, a powerful operation but a fundamentally *deterministic* one. The same query always produces the same output. Attention retrieves; it does not generate. Yet generation from a structured memory is precisely what many downstream tasks require: producing novel but plausible continuations, interpolating between stored prototypes, or exploring the space of patterns consistent with partial evidence. A natural question arises: *can the attention mechanism itself be made stochastic, in a principled way, so that it samples from the space of memories rather than merely returning their weighted average?*

The ingredients for an answer already exist, though they have not been assembled. On one side, a line of work on associative memory, from Hopfield networks [2] through dense associative memories [3, 4] to the modern continuous formulation of Ramsauer et al. [5], has revealed that each attention head implicitly performs gradient descent on a smooth, confining energy whose minima are stored patterns. On the other side, a mature theory of Langevin dynamics [6–8] shows how to convert *any* such energy into a sampler for the corresponding Boltzmann distribution: one simply adds calibrated noise to the gradient update. Meanwhile, energy-based models [9, 10] and score-based diffusion methods [11, 12]

---

\*Repository: <https://github.com/varnerlab/stochastic-attention-study-paper.git>.

have demonstrated the power of Langevin-type sampling for generation, but rely on black-box neural networks whose scores must be learned. The Energy Transformer [13] brings Hopfield energies into a deep architecture, yet remains a discriminative model that descends the energy rather than sampling from it. The classical retrieval-generation duality (Hopfield networks retrieve, Boltzmann machines sample, and both are defined by the same quadratic interaction energy over binary states [14]) has not been lifted to the modern continuous setting.

In this paper, we close that gap. We show that applying the unadjusted Langevin algorithm to the modern Hopfield energy yields a *stochastic attention* update: a single iteration comprising a contraction toward the origin, a softmax attention pull toward stored memories, and an isotropic Gaussian perturbation whose magnitude is governed by the temperature. The inverse temperature  $\beta$  interpolates continuously between exact retrieval ( $\beta \rightarrow \infty$ ) and open-ended exploration ( $\beta \rightarrow 0$ ), providing a principled generation mechanism that requires no learned score network, no training loop, and no contrastive objective. Because the gradient of the Hopfield energy is exactly the identity minus the attention map, every step of the sampler is computed by the same primitive operations as a standard attention head. In particular,  $\mathbf{X}$  can be the key matrix of any pretrained attention layer, making stochastic attention a zero-shot stochastic decoding layer. When the attention head uses learned  $Q, K, V$  projections operating on hidden states rather than raw patterns, the connection requires projecting through these learned transformations; we leave this extension, along with applications to retrieval-augmented generation and in-context learning, to future work. The energy’s analytic structure (infinite differentiability, Lipschitz gradients, and a quadratic confining bound) delivers convergence guarantees that generic energy-based models cannot offer without additional assumptions. In practice, the same algorithm realizes two qualitatively distinct operating regimes: at high  $\beta$  it performs *structured retrieval*, generating outputs that closely resemble stored patterns; once  $\beta$  falls below a critical signal-to-noise ratio  $\text{SNR}^*$  whose scaling is derived from the entropy inflection of the attention distribution (Section 4), it performs *genuine generation*, producing novel outputs that outperform learned baselines on both novelty and diversity while preserving domain-level fidelity (e.g.,  $6.9\times$  lower amino acid composition divergence than a VAE on protein sequences). The individual ingredients, the Hopfield energy gradient [5] and the Langevin algorithm [6], are known. The contribution lies in their synthesis and in the analysis it enables, which is inaccessible from either ingredient alone. First, because the Hopfield energy gradient is exactly the identity minus the attention map, the score function is available in closed form at the cost of a single attention evaluation; this eliminates the score matching or contrastive divergence required by standard energy-based and score-based generative models, and converts any pretrained attention head into a sampler with no additional training. Second, Ramsauer et al. studied the energy only for retrieval ( $\beta \rightarrow \infty$ ) and the Langevin literature does not know about attention; by analyzing the energy *as a sampling target* we characterize the full temperature spectrum, and the entropy inflection analysis (Proposition 3) identifies the critical  $\beta^*$  at which the sampler transitions from retrieval to generation, with a scaling law  $\beta^* \sim \sqrt{d}$  that yields a dimension-dependent SNR criterion for temperature selection. Third, the smoothness, dissipativity, and condition number of the Hopfield energy as a function of  $\beta$  and  $K/d$  had not been characterized for the purpose of sampling guarantees; we provide these bounds (Proposition 1) and show where they apply and where they break down. Section 2 surveys related work; Section 3 reviews the necessary background on attention, modern Hopfield networks, and Langevin dynamics; Section 4 derives the stochastic attention update, presents the algorithm, and characterizes its properties; Section 5 validates both regimes experimentally across five domains.

## 2 Related Work

Our work lies at the intersection of associative memory, energy-based modeling, and Langevin sampling. We review each strand and identify where existing approaches stop short of the connection we propose.

**Hopfield networks and associative memory.** Hopfield [2] introduced a recurrent network of  $d$  binary neurons whose asynchronous dynamics minimize the quadratic energy  $E(\mathbf{s}) = -\frac{1}{2}\mathbf{s}^\top \mathbf{W}\mathbf{s}$ , with  $\mathbf{W} = \frac{1}{d}\sum_i \mathbf{m}_i \mathbf{m}_i^\top$  the Hebbian weight matrix. Stored patterns correspond to local minima of  $E$ , so retrieval proceeds by gradient descent from an initial probe. When the  $K$  patterns are uncorrelated random binary vectors, Amit et al. [15] showed via a replica-symmetric mean-field analysis that reliable retrieval is possible only when the load ratio  $K/d < \alpha_c \approx 0.138$  (where  $\alpha_c$  denotes the critical load ratio, not to be confused with the step size  $\alpha$  used later); beyond this threshold

the energy landscape becomes dominated by spurious mixtures. Folli et al. [16] later gave exact finite- $d$  expressions for the bit-error probability, confirming the  $\alpha_c$  transition and showing that the number of retrieval errors grows with  $K/d$  as cross-talk noise overwhelms the coherent signal.

The modern Hopfield network program, initiated by Krotov and Hopfield [3], addresses these shortcomings by replacing the quadratic interaction with higher-order (polynomial or exponential) interaction functions. Dense associative memories with degree- $n$  polynomial energy store on the order of  $d^{n-1}$  patterns, breaking the linear capacity barrier by trading pairwise for higher-order synaptic interactions, and the resulting retrieval dynamics map onto deep networks with rectified polynomial activations. At the top of this hierarchy sits the log-sum-exp (lse) energy, which achieves storage capacity that grows *exponentially* in the pattern dimension  $d$  [5]. Ramsauer et al. [5] proved that the continuous-state retrieval map associated with the lse energy is equivalent to transformer-style attention: each attention head performs one step of gradient descent on the energy, and the fixed points of the dynamics (global, metastable, or single-pattern) correspond to different retrieval regimes. All of these works, however, focus exclusively on *retrieval*, that is, the convergence of iterates to stored patterns or their convex combinations. Sampling from the Boltzmann distribution defined by the same energy, which would yield a generative mechanism, is not explored. Our work fills this gap by applying Langevin dynamics to the modern Hopfield energy, converting the deterministic retrieval map into a stochastic sampler.

The idea that a single energy function supports both retrieval and generation dates to the Boltzmann machine [14], which shares the quadratic energy of the Hopfield network but samples from it via Gibbs dynamics instead of minimizing it. Sejnowski [17] extended this to higher-order interactions, corresponding to the polynomial energies later studied by Krotov and Hopfield [3]. However, these classical models operate on binary states with discrete Gibbs sampling; our formulation inherits the same duality in the continuous, modern Hopfield setting where Langevin dynamics scales naturally to high dimensions.

**Energy-based, score-based and diffusion models.** Energy-based models (EBMs) define a probability distribution  $p(\mathbf{x}) \propto \exp(-E(\mathbf{x}))$  for an energy function  $E$  parameterized by a neural network [9]. Training typically proceeds by contrastive divergence [18], score matching [19], or noise contrastive estimation [20, 10]. The energy in a generic EBM is a black-box neural network, so its gradient (the score function) must be estimated or approximated. By contrast, the modern Hopfield energy has a *closed-form* gradient (identity minus softmax attention) requiring no auxiliary score network. Moreover,  $\mathbf{X}$  is given as data rather than learned, so no training loop is needed, and the log-sum-exp structure provides analytic guarantees (smoothness, Lipschitz gradients, quadratic confinement) that generic EBMs achieve only with careful architectural design. The Energy Transformer [13] shows that Hopfield-type energies improve discriminative tasks (graph anomaly detection, image completion) but does not sample from the Boltzmann distribution; our work uses the same energy class for generation.

Song and Ermon [11] introduced score-based generative modeling, in which a neural network is trained to approximate  $\nabla \log p(\mathbf{x})$  at multiple noise levels, and samples are drawn by annealed Langevin dynamics. Song et al. [12] unified this framework with diffusion probabilistic models [21, 22] by showing that both arise from forward and reverse-time stochastic differential equations. These methods achieve remarkable sample quality but rely on a learned score network trained on data; our score function is *exact* and *analytic*,  $\nabla \log p_\beta(\boldsymbol{\xi}) = \beta(\mathbf{T}(\boldsymbol{\xi}) - \boldsymbol{\xi})$ , requiring no training, at the cost of being restricted to the Boltzmann distribution of a fixed memory  $\mathbf{X}$ , a restriction that permits convergence guarantees unavailable in the learned-score setting.

Normalizing flows [23] construct flexible generative models via learned invertible transformations; like diffusion models, they require training data and a learned bijection, and do not expose a closed-form score function over a fixed memory. Several works have introduced stochasticity into the attention mechanism itself: Deng et al. [24] replace the softmax with a latent categorical or Gaussian variable, trained via variational inference, to model alignment uncertainty in sequence-to-sequence tasks. These approaches treat attention weights as random variables to be inferred, whereas our stochasticity arises from Langevin dynamics on a fixed Hopfield energy: the temperature parameter  $1/\beta$  controls the noise level, no variational objective is optimized, and the goal is memory-based generation rather than alignment uncertainty.

### 3 Background

We build our approach on three ideas that, taken separately, are well understood but whose intersection has not been explored. We review them here in the order that motivates our construction: attention as a computational primitive, its reinterpretation as energy minimization via modern Hopfield networks, and Langevin dynamics as the tool that converts any energy landscape into a sampler.

**Attention as deterministic retrieval.** The transformer architecture [1] computes attention via queries  $\mathbf{Q}$ , keys  $\mathbf{K}$ , and values  $\mathbf{V}$ :

$$\text{Attention}(\mathbf{Q}, \mathbf{K}, \mathbf{V}) = \text{softmax}\left(\frac{\mathbf{Q}\mathbf{K}^\top}{\sqrt{d}}\right) \mathbf{V}, \quad (1)$$

where  $d$  is the key dimension and the softmax is applied row-wise. Each output row is a convex combination of value vectors, with weights determined by query-key similarity. Crucially, this operation is *deterministic*: given the same query, it always returns the same weighted average. Attention retrieves information from a fixed store; it does not generate anything new. Our goal is to relax this limitation, but to do so we first need to understand what energy landscape attention is implicitly descending.

**The energy landscape beneath attention.** The classical Hopfield network [2] stores  $K$  binary patterns  $\mathbf{m}_1, \dots, \mathbf{m}_K \in \{-1, +1\}^d$  via the quadratic energy

$$E_{\text{classical}}(\mathbf{s}) = -\frac{1}{2} \mathbf{s}^\top \mathbf{W} \mathbf{s} - \mathbf{b}^\top \mathbf{s}, \quad \mathbf{W} = \frac{1}{d} \sum_{i=1}^K \mathbf{m}_i \mathbf{m}_i^\top, \quad (2)$$

where  $\mathbf{b} \in \mathbb{R}^d$  is an external bias (typically set to zero). Retrieval proceeds by coordinate-wise sign updates that descend  $E_{\text{classical}}$ . The storage capacity of this network scales as  $\mathcal{O}(d)$  [15], severely limiting the number of patterns.

*Modern* (continuous) Hopfield networks [5] overcome this bottleneck by replacing the quadratic energy with a log-sum-exp (lse) form. Let  $\mathbf{X} = [\mathbf{m}_1, \dots, \mathbf{m}_K] \in \mathbb{R}^{d \times K}$  be the memory matrix,  $\beta > 0$  an inverse temperature, and  $M := \max_i \|\mathbf{m}_i\|_2$ . The energy is

$$E(\boldsymbol{\xi}) = -\text{lse}_\beta(\mathbf{X}^\top \boldsymbol{\xi}) + \frac{1}{2} \|\boldsymbol{\xi}\|_2^2 + \frac{1}{\beta} \log K + \frac{1}{2} M^2, \quad (3)$$

where  $\text{lse}_\beta(\mathbf{z}) := \beta^{-1} \log(\sum_{i=1}^K e^{\beta z_i})$  is the scaled log-sum-exp. The associated retrieval (update) map is

$$\mathbf{T}(\boldsymbol{\xi}) := \mathbf{X} \text{softmax}(\beta \mathbf{X}^\top \boldsymbol{\xi}), \quad (4)$$

and one can show that  $\nabla E(\boldsymbol{\xi}) = \boldsymbol{\xi} - \mathbf{T}(\boldsymbol{\xi})$  [5]. Hence the deterministic iteration  $\boldsymbol{\xi}^{t+1} = \mathbf{T}(\boldsymbol{\xi}^t)$  is gradient descent on  $E$  with unit step size, converging to a fixed point  $\boldsymbol{\xi}^*$  satisfying  $\mathbf{T}(\boldsymbol{\xi}^*) = \boldsymbol{\xi}^*$ .

Two properties of this energy are essential for what follows. First,  $E$  is  $C^\infty$  (the lse is infinitely differentiable), so standard gradient-based convergence theory applies. Second,  $E$  is *confining*: it admits the lower bound [5]

$$E(\boldsymbol{\xi}) \geq \frac{1}{2} (\|\boldsymbol{\xi}\|_2 - M)^2 \geq 0, \quad (5)$$

so  $E$  grows at least quadratically as  $\|\boldsymbol{\xi}\| \rightarrow \infty$ . Iterates cannot escape to infinity.

**The bridge.** Ramsauer et al. [5] observed that single-head attention (1) with  $\mathbf{Q} = \boldsymbol{\xi}^\top$ ,  $\mathbf{K} = \mathbf{X}^\top$ ,  $\mathbf{V} = \mathbf{X}^\top$ , and inverse temperature  $\beta = 1/\sqrt{d}$  is *exactly one step* of the retrieval map (4). In other words, every attention head is implicitly performing energy minimization on (3), revealing a hidden energy landscape whose minima are the stored memories.

**From minimization to sampling.** Given a smooth potential  $U : \mathbb{R}^d \rightarrow \mathbb{R}$  with target density  $p(\mathbf{x}) \propto \exp(-U(\mathbf{x}))$ , the (overdamped) Langevin stochastic differential equation is

$$d\mathbf{x}_t = -\nabla U(\mathbf{x}_t) dt + \sqrt{2} d\mathbf{B}_t, \quad (6)$$

where  $\mathbf{B}_t$  is standard  $d$ -dimensional Brownian motion. The process (6) has  $p$  as its unique stationary distribution provided two regularity conditions hold [6]: **(R1)**  $\nabla U$  is  $L$ -Lipschitz, i.e.  $\|\nabla U(\mathbf{x}) -$

$\|\nabla U(\mathbf{y})\|_2 \leq L\|\mathbf{x} - \mathbf{y}\|_2$ ; and **(R2)**  $U$  is dissipative, i.e.  $\langle \nabla U(\mathbf{x}), \mathbf{x} \rangle \geq a\|\mathbf{x}\|_2^2 - b$  for constants  $a > 0, b \geq 0$ . The modern Hopfield energy (3) satisfies both: it is  $C^\infty$  with Lipschitz gradient **(R1)**, and its quadratic lower bound (5) implies dissipativity **(R2)**.

In practice, we discretize (6) with step size  $\alpha > 0$  to obtain the *unadjusted Langevin algorithm* (ULA) [6]:

$$\mathbf{x}_{t+1} = \mathbf{x}_t - \alpha \nabla U(\mathbf{x}_t) + \sqrt{2\alpha} \boldsymbol{\epsilon}_t, \quad \boldsymbol{\epsilon}_t \sim \mathcal{N}(\mathbf{0}, \mathbf{I}). \quad (7)$$

The noise scale  $\sqrt{2\alpha}$  maintains the *fluctuation-dissipation relation* so that, in the limit  $\alpha \rightarrow 0$ , iterates sample exactly from  $p$  [7]. For finite  $\alpha$  the stationary distribution is biased, but the bias vanishes as  $\alpha \rightarrow 0$  and can be bounded when  $U$  is smooth and strongly convex outside a ball [8]. Introducing an inverse temperature  $\beta > 0$  via  $U = \beta E$  yields a Boltzmann target  $p_\beta \propto \exp(-\beta E)$ ; the temperature  $1/\beta$  controls the trade-off between exploitation (retrieval) and exploration (generation). Section 4 makes this connection explicit.

## 4 Method

The background section established three facts: (i) attention is one step of gradient descent on the modern Hopfield energy  $E$ , (ii)  $E$  is smooth and confining, and (iii) Langevin dynamics converts any smooth, confining energy into a sampler for the corresponding Boltzmann distribution. We now combine these facts to derive *stochastic attention*, a single update rule that interpolates between deterministic memory retrieval and stochastic generation of novel states.

### 4.1 Stochastic Attention Update

Recall the setup from Section 3: the memory matrix  $\mathbf{X} = [\mathbf{m}_1, \dots, \mathbf{m}_K] \in \mathbb{R}^{d \times K}$  has  $K$  stored memories as its columns, each of dimension  $d$ . We wish to sample from the Boltzmann distribution induced by the modern Hopfield energy (3):

$$p_\beta(\boldsymbol{\xi}) \propto \exp(-\beta E(\boldsymbol{\xi})), \quad (8)$$

where  $\beta > 0$  is the inverse temperature and  $E$  is defined in (3). To apply the ULA (7) we need  $\nabla E$ . The background already established the identity  $\nabla E(\boldsymbol{\xi}) = \boldsymbol{\xi} - \mathbf{T}(\boldsymbol{\xi})$ , where  $\mathbf{T}$  is the softmax attention map (4). Applying the ULA to the potential  $U = \beta E$  with step size  $\tilde{\alpha}$  gives  $\boldsymbol{\xi}_{t+1} = \boldsymbol{\xi}_t - \tilde{\alpha} \nabla U + \sqrt{2\tilde{\alpha}} \boldsymbol{\epsilon}_t$ . Substituting  $\tilde{\alpha} = \alpha/\beta$  (so the effective step for  $\nabla E$  is  $\alpha$  and the noise scale becomes  $\sqrt{2\alpha/\beta}$ ), we obtain

$$\boldsymbol{\xi}_{t+1} = \boldsymbol{\xi}_t - \alpha(\boldsymbol{\xi}_t - \mathbf{T}(\boldsymbol{\xi}_t)) + \sqrt{\frac{2\alpha}{\beta}} \boldsymbol{\epsilon}_t, \quad \boldsymbol{\epsilon}_t \sim \mathcal{N}(\mathbf{0}, \mathbf{I}), \quad (9)$$

which, after collecting terms, takes the form

$$\boxed{\boldsymbol{\xi}_{t+1} = (1 - \alpha) \boldsymbol{\xi}_t + \alpha \mathbf{X} \operatorname{softmax}(\beta \mathbf{X}^\top \boldsymbol{\xi}_t) + \sqrt{\frac{2\alpha}{\beta}} \boldsymbol{\epsilon}_t} \quad (10)$$

This is the *stochastic attention* update. Each iteration performs three operations: a contraction toward the origin (the  $(1 - \alpha)\boldsymbol{\xi}_t$  term), a softmax-weighted pull toward stored memories (the attention term), and an isotropic Gaussian perturbation whose magnitude is governed by the temperature  $1/\beta$ . The complete procedure is given as pseudocode in Algorithm 1. Because the memory matrix  $\mathbf{X}$  is fixed and known, each step requires only the same primitive operations as a single attention head: two matrix-vector products, one softmax, and one Gaussian draw, for a per-step cost of  $\mathcal{O}(dK)$ .

### 4.2 Properties and Limiting Behavior

The update (10) is controlled by two parameters, the inverse temperature  $\beta$  and the step size  $\alpha$ , that together determine where the sampler sits on a spectrum from exact retrieval to open-ended generation.

When  $\beta \rightarrow \infty$  and the noise vanishes, the softmax sharpens to a hard arg max and the update reduces to deterministic retrieval of the nearest stored memory (*hard attention*). At finite  $\beta$  with zero noise, the update yields the standard softmax-weighted average familiar from transformers (*soft attention*). When  $\beta$  is finite and noise is present, the sampler generates states that fluctuate around

---

**Algorithm 1** Stochastic Attention Sampler

---

**Require:** Memory matrix  $\mathbf{X} \in \mathbb{R}^{d \times K}$ , inverse temperature  $\beta > 0$ , step size  $\alpha \in (0, 1)$ , number of iterations  $T$ , initial state  $\xi_0 \in \mathbb{R}^d$   
**Ensure:** Sample trajectory  $\xi_0, \xi_1, \dots, \xi_T$   
1: **for**  $t = 0, 1, \dots, T - 1$  **do**  
2:    $\mathbf{a}_t \leftarrow \text{softmax}(\beta \mathbf{X}^\top \xi_t)$  ▷ attention weights  
3:    $\epsilon_t \sim \mathcal{N}(\mathbf{0}, \mathbf{I}_d)$   
4:    $\xi_{t+1} \leftarrow (1 - \alpha) \xi_t + \alpha \mathbf{X} \mathbf{a}_t + \sqrt{2\alpha/\beta} \epsilon_t$   
5: **end for**

---

stored memories, producing novel patterns shaped by the memory geometry (*stochastic attention*). As  $\beta \rightarrow 0$ , the Boltzmann distribution flattens and sampling becomes noise-dominated. The step size  $\alpha \in (0, 1)$  controls discretization fidelity: smaller  $\alpha$  reduces ULA bias [8] at the cost of slower mixing, while larger  $\alpha$  accelerates exploration but increases discretization error.

Beyond these limiting behaviors, the sampler inherits concrete guarantees from the analytic structure of the Hopfield energy. Because the gradient  $\nabla E(\xi) = \xi - \mathbf{T}(\xi)$  is computed exactly by a single attention operation, the score function  $\nabla \log p_\beta = \beta(\mathbf{T} - \xi)$  is known in closed form; no auxiliary score network is needed. The following proposition (proved in Appendix B) makes the regularity conditions from Section 3 explicit.

**Proposition 1.** *Let  $\sigma_{\max} = \|\mathbf{X}\|_{\text{op}}$  denote the largest singular value of the memory matrix. The modern Hopfield energy (3) has Lipschitz-continuous gradient with constant  $L = 1 + \beta\sigma_{\max}^2/2$  and satisfies the dissipativity condition  $\langle \nabla E(\xi), \xi \rangle \geq \|\xi\|_2^2/2 - M^2/2$  for all  $\xi \in \mathbb{R}^d$ .*

The Lipschitz constant grows linearly in  $\beta$ : the energy landscape sharpens at low temperature and step-size selection becomes more delicate. The Hessian satisfies  $\nabla^2 E \succeq (1 - \beta\sigma_{\max}^2/2)\mathbf{I}$ , so  $E$  is strictly convex when  $\beta\sigma_{\max}^2 < 2$ . This condition characterizes the *convex regime* of the Hopfield energy and yields a standard ULA convergence result:

**Corollary 2.** *When  $\beta\sigma_{\max}^2 < 2$ , the potential  $U = \beta E$  is  $m$ -strongly convex with  $m = \beta(1 - \beta\sigma_{\max}^2/2)$  and has  $L_U$ -Lipschitz gradient with  $L_U = \beta(1 + \beta\sigma_{\max}^2/2)$ . The iterates of Algorithm 1 then converge to  $p_\beta$  in  $W_2$  at a geometric rate, with a discretization bias that vanishes as  $\alpha \rightarrow 0$  [25, 8].*

**Beyond the convex regime.** Corollary 2 applies when  $\beta\sigma_{\max}^2 < 2$ . In our experiments  $\sigma_{\max}^2 \approx 2-3$ , so this condition holds only for  $\beta \lesssim 1$ , well below the operating range ( $\beta \in \{200, 2000\}$ ). We state this boundary explicitly because it delineates where the Hopfield energy transitions from unimodal (one global basin) to multimodal (one local minimum per stored pattern): the condition  $\beta\sigma_{\max}^2 = 2$  is the onset of non-convexity, beyond which energy barriers separate stored memories.

Proving mixing-time bounds in the multimodal regime ( $\beta\sigma_{\max}^2 > 2$ ) is a fundamental open problem, not specific to our setting. For general non-convex energies, the mixing time of Langevin dynamics scales exponentially in the barrier height divided by the temperature [26]. In the Hopfield energy at high  $\beta$ , the barriers between stored patterns are  $O(\beta)$  while the temperature is  $1/\beta$ , so inter-basin mixing is exponentially slow. This is consistent with our empirical observation that a single chain at  $\beta=2000$  does not cross between basins (single-chain diversity 0.282; Appendix F).

However, the practical situation is more favorable than the worst-case theory suggests. Within a single basin the energy is locally strongly convex (the Hessian near each minimum is positive definite), so *intra-basin* mixing is fast. The multi-chain protocol (Section 5) is designed to exploit this: by initializing 30 chains near distinct stored patterns, we obtain coverage across basins through initialization and rely on fast local mixing within each basin. At  $\beta=200$ , the barriers are low enough that single chains do cross basins (single-chain diversity 0.796, exceeding the multi-chain  $\beta=2000$  value of 0.600).

Two guarantees hold for all  $\beta > 0$  regardless of convexity. First, the continuous-time Langevin SDE is geometrically ergodic by the dissipativity of Proposition 1 [6], ensuring convergence to the correct Boltzmann target (though without an explicit rate). Second, the MALA acceptance rate of 99.2% at  $\alpha=0.01$  (Table 1) confirms that ULA discretization bias is negligible in practice, and the step-size sweep (Appendix K) maps where this approximation breaks down.

Because  $\mathbf{X}$  is given as data, there are no learned parameters: no training loop, no contrastive divergence, and no score-matching objective. The confining bound (5) keeps iterates concentrated near  $\text{conv}\{\mathbf{m}_1, \dots, \mathbf{m}_K\}$  with excursions controlled by  $\sqrt{2\alpha/\beta}$ ; Section 4.3 derives a  $\beta$ -selection rule from the entropy of the attention distribution.

### 4.3 Phase Transition and Temperature Selection

The attention entropy  $H(\beta) = -\sum_k p_k \log p_k$ , where  $p_k = \text{softmax}(\beta \mathbf{X}^\top \boldsymbol{\xi})_k$ , quantifies the selectivity of the attention distribution for a given state  $\boldsymbol{\xi}$ . At  $\beta = 0$  the distribution is uniform and  $H = \log K$ ; as  $\beta \rightarrow \infty$  it concentrates on the nearest memory and  $H \rightarrow 0$ . The following identity governs the rate of this transition.

**Proposition 3.** For fixed  $\boldsymbol{\xi} \in \mathbb{R}^d$ , let  $e_k = \mathbf{m}_k^\top \boldsymbol{\xi}$  and  $\mathbf{p} = \text{softmax}(\beta \mathbf{e})$ . Then

$$\frac{dH}{d\beta} = -\beta \text{Var}_{\mathbf{p}}(e), \quad (11)$$

where  $\text{Var}_{\mathbf{p}}(e) = \sum_k p_k e_k^2 - (\sum_k p_k e_k)^2$ .

*Proof.* Write  $\log p_k = \beta e_k - \log Z$  with  $Z = \sum_j \exp(\beta e_j)$ , so that  $H = -\beta \langle e \rangle_{\mathbf{p}} + \log Z$ . Differentiating and using the standard identities  $d(\log Z)/d\beta = \langle e \rangle_{\mathbf{p}}$  and  $d\langle e \rangle_{\mathbf{p}}/d\beta = \text{Var}_{\mathbf{p}}(e)$  yields the result.  $\square$

Since  $\text{Var}_{\mathbf{p}}(e) \geq 0$ , entropy decreases monotonically with  $\beta$ . At  $\beta = 0$  the derivative vanishes because the prefactor  $\beta$  is zero; as  $\beta \rightarrow \infty$  it again vanishes because the variance collapses. The maximum rate of entropy loss therefore occurs at an intermediate *inflection point*  $\beta^*$  satisfying  $d^2 H/d\beta^2 = 0$ :

$$\text{Var}_{\mathbf{p}}(e)|_{\beta^*} = -\beta^* \mu_3|_{\beta^*}, \quad (12)$$

where  $\mu_3 = \langle (e - \langle e \rangle_{\mathbf{p}})^3 \rangle_{\mathbf{p}}$  is the third central moment of the similarities under the attention distribution. This inflection point marks the retrieval-generation phase boundary: below  $\beta^*$ , attention remains diffuse (generation); above it, attention concentrates on individual memories (retrieval).

**Scaling for random memories.** When the  $K$  memories are drawn uniformly on the unit sphere  $\mathbb{S}^{d-1}$ , the similarities  $e_k$  are approximately iid with  $\text{Var}(e_k) = 1/d$ . The softmax logits  $\beta e_k$  have standard deviation  $\beta/\sqrt{d}$ ; the transition from near-uniform to concentrated attention occurs when this standard deviation reaches order unity, giving

$$\beta^* \sim \sqrt{d}. \quad (13)$$

Substituting into the per-step signal-to-noise ratio (Eq. 15) yields a scaling law for the critical SNR:

$$\text{SNR}^* = \sqrt{\frac{\alpha \beta^*}{2d}} \sim \sqrt{\frac{\alpha}{2\sqrt{d}}}. \quad (14)$$

At  $d=64$  and  $\alpha=0.01$  this evaluates to  $\text{SNR}^* = \sqrt{0.01/16} = 0.025$ , exactly matching the empirical transition observed in Section 5. The threshold is not a universal constant: it scales as  $d^{-1/4}$  and depends on the pattern geometry through  $\text{Var}(e_k)$ . For structured data the effective variance may differ substantially from  $1/d$ , but Eq. (12) provides a fully data-dependent criterion that applies in any domain: evaluate  $d^2 H/d\beta^2$  over a sweep of  $\beta$  values and locate the zero crossing.

## 5 Experiments

**Temperature spectrum, Convergence diagnostics and Load Ratio using synthetic data.** For the first three experiments we constructed memory matrices whose columns are independent draws from the uniform distribution on the unit sphere  $\mathbb{S}^{d-1}$ . Concretely, each pattern was sampled as  $\mathbf{x}_k \sim \mathcal{N}(\mathbf{0}, \mathbf{I}_d)$  and normalized,  $\mathbf{x}_k \leftarrow \mathbf{x}_k / \|\mathbf{x}_k\|$ . This is the standard generative model in the Hopfield capacity literature [15, 16] and ensures that, in expectation, the  $K$  patterns are nearly orthogonal for moderate load ratios  $K/d$ . Unless otherwise noted we fixed  $d = 64$ ; the convergence

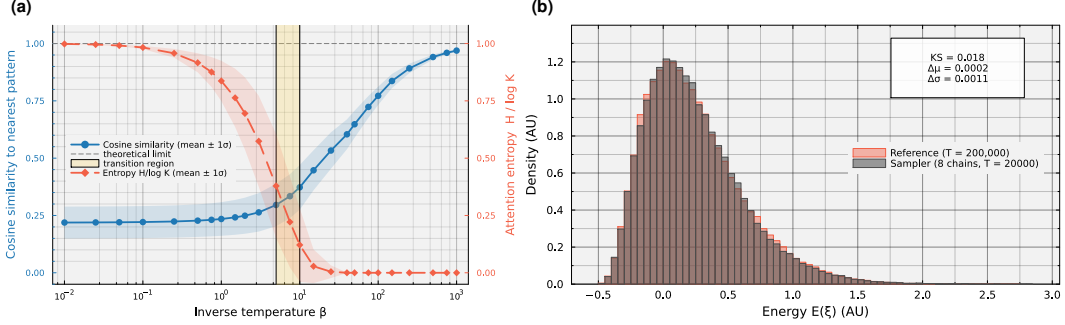


Figure 1: Synthetic experiments. **(a)** Phase behavior as a function of inverse temperature  $\beta$  ( $d = 64$ ,  $K = 16$ ). Left axis (blue): mean cosine similarity to the nearest stored pattern; right axis (coral): scaled entropy  $H(\mathbf{a})/\log K$ . Both diagnostics reveal a smooth transition centered near  $\beta \approx 5$ – $10$  (gold band). **(b)** Convergence validation ( $d = 8$ ,  $K = 4$ ,  $\beta = 5$ ). Pooled energy density from eight independent chains (gray) overlaid on a long-run reference distribution (coral); inset reports the Kolmogorov–Smirnov statistic and moment differences.

experiment used  $d = 8$  so that the Boltzmann target density remained tractable for ground-truth comparison. All datasets were generated with fixed random seeds.

We evaluated how the inverse temperature  $\beta$  controlled the transition from noise-dominated diffusion to near-deterministic retrieval (Fig. 1a). We stored  $K = 16$  unit-norm patterns in  $\mathbf{X} \in \mathbb{R}^{64 \times 16}$  and ran Algorithm 1 for  $T = 10,000$  iterations at each of 25 values of  $\beta$  spanning the range  $[10^{-2}, 10^3]$  (approximately log-spaced), with step size  $\alpha = 0.01$  and a burn-in of 2,000 samples. For every post-burn-in sample  $\xi_t$  we recorded two diagnostics: the cosine similarity to the nearest stored pattern,  $\max_k \mathbf{m}_k^\top \xi_t / (\|\mathbf{m}_k\| \|\xi_t\|)$ , and the Shannon entropy of the attention weights,  $H(\mathbf{p}) = -\sum_k p_k \log p_k$  where  $\mathbf{p} = \text{softmax}(\beta \mathbf{X}^\top \xi_t)$ .

Both curves exhibited a smooth sigmoidal transition centered near  $\beta \approx 5$ – $10$ . At small  $\beta$  the cosine similarity plateaued around 0.22, consistent with the expected inner product between a random unit vector and 16 stored patterns in 64 dimensions, while the entropy saturated at  $\log K \approx 2.77$  nats, the uniform limit. As  $\beta$  increased through the transition region the attention weights concentrated on a single pattern: the entropy dropped sharply to zero by  $\beta \approx 25$ , and the cosine similarity rose to 0.969 at  $\beta = 1000$ . The variance of both diagnostics peaked in the transition region, where the chain intermittently switched between pattern-aligned and exploratory states. These results confirmed that  $\beta$  acts as a continuous order parameter interpolating between disordered and ordered phases, in direct analogy to the paramagnetic-to-ferromagnetic transition in classical Hopfield networks [14]; the useful generation regime occupies intermediate  $\beta$  values whose scale is problem-dependent and set by the SNR argument of Eq. (15).

We verified that Algorithm 1 converged to the correct Boltzmann target by running multiple independent chains on a small system where thorough mixing is feasible (Fig. 1b). We stored  $K = 4$  unit-norm patterns in  $\mathbf{X} \in \mathbb{R}^{8 \times 4}$  and launched eight chains from different random initializations at  $\beta = 5$  with step size  $\alpha = 0.01$  and  $T = 20,000$  iterations, discarding the first 5,000 steps as burn-in. All eight chains converged to the same stationary energy level; pooled post-burn-in energies closely matched a long-chain reference distribution ( $T = 200,000$ , burn-in 50,000) with a small KS statistic, confirming convergence to the correct Boltzmann target rather than a single mode.

We mapped the joint effect of memory load and temperature on attention selectivity by constructing a phase diagram over the load ratio  $K/d$  and inverse temperature  $\beta$  (Fig. 3). We set  $d = 64$  and swept  $K/d$  across 10 values in  $[0.05, 2.0]$  and  $\beta$  across 20 log-spaced values in  $[0.5, 100]$ , running Algorithm 1 on five independent datasets per condition with  $T = 10,000$  iterations, step size  $\alpha = 0.01$ , and a burn-in of 2,000. For each  $(\beta, K/d)$  pair we reported the attention concentration  $C = 1 - H(\mathbf{a})/\log K$ , averaged over post-burn-in samples and datasets;  $C = 1$  indicates perfect pattern-selective attention and  $C = 0$  the uniform limit. The resulting heatmap revealed a clear phase boundary (dashed  $C = 0.5$  contour): a retrieval regime in the upper-left corner (high  $\beta$ , low  $K/d$ ) where the sampler locked onto individual patterns, and a diffuse regime in the lower-right where attention spread uniformly across all memories. The boundary shifted rightward as  $\beta$  increased,

indicating that higher inverse temperature extends reliable retrieval to larger memory loads, consistent with classical Hopfield capacity theory [15].

**Image generation on MNIST.** The synthetic experiments above validated the sampler’s statistical properties on controlled data. We tested whether it could generate structured, recognizable outputs from real-world patterns and compared it against seven baselines. We selected  $K = 100$  images of the digit “3” from the MNIST training set [27], flattened each to a vector in  $\mathbb{R}^{784}$ , and normalized to unit norm to form the memory matrix  $\mathbf{X} \in \mathbb{R}^{784 \times 100}$  (load ratio  $K/d \approx 0.13$ ). Because the energy landscape at high  $\beta$  is deeply multimodal, a single long chain can become trapped in one basin for the entire run. We therefore launched 30 independent chains, each initialized near a different randomly chosen stored pattern with a small Gaussian perturbation ( $\sigma_{\text{init}} = 0.01$ ). Each chain ran Algorithm 1 at  $\beta = 2000$  with step size  $\alpha = 0.01$  for  $T = 5,000$  iterations; after discarding the first 2,000 steps as burn-in, thinning every 100th iteration to obtain 30 post-burn-in snapshots, and sub-sampling 5 evenly spaced snapshots per chain, we retained  $30 \times 5 = 150$  generated images that collectively span 30 distinct energy basins.

The choice of  $\beta = 2000$  follows from the phase transition analysis of Section 4.3. The per-step signal-to-noise ratio,

$$\text{SNR} = \frac{O(\alpha)}{\sqrt{2\alpha d/\beta}} = \sqrt{\frac{\alpha\beta}{2d}}, \quad (15)$$

where numerator and denominator are the gradient displacement and expected noise magnitude, undergoes a critical transition at  $\text{SNR}^* = \sqrt{\alpha/(2\sqrt{d})}$  (Eq. 14), the entropy inflection point of Proposition 3. At  $d=64$  and  $\alpha=0.01$ , this gives  $\text{SNR}^* = 0.025$  ( $\beta^* \approx 8$ ), consistent with the observed transition at  $\beta \approx 5\text{--}10$ . For structured data the effective dimensionality is lower and the transition  $\beta$  shifts accordingly; we set  $\beta = 2000$  ( $\text{SNR} = 0.113$ ) to operate well inside the structured-retrieval regime.

To isolate the contribution of the energy-landscape structure, we compared against seven baselines that used the same memory matrix: (i) *bootstrap resampling*, which draws a stored pattern uniformly at random; (ii) *Gaussian perturbation*, which selects a random stored pattern and adds isotropic noise  $\mathcal{N}(\mathbf{0}, \sigma^2 \mathbf{I})$  with  $\sigma$  matched to the sampler’s per-step noise scale  $\sqrt{2\alpha/\beta}$ ; (iii) *random convex combination*, which outputs  $\mathbf{X}\mathbf{w}$  for weights  $\mathbf{w} \sim \text{Dirichlet}(1, \dots, 1)$ ; (iv) *GMM-PCA*, which projects the  $K$  patterns onto the top-50 PCA components, fits a 10-component diagonal-covariance GMM via EM, and draws samples from the learned distribution (full specification in Appendix J.1); (v) *VAE* [28] (latent dim 8, encoder  $784 \rightarrow 256 \rightarrow 128 \rightarrow \mu/\log \sigma^2$ , decoder symmetric), trained for 4,000 epochs on the same  $K=100$  patterns with two-phase training to avoid posterior collapse, samples from  $\mathcal{N}(\mathbf{0}, \mathbf{I})$  (full specification in Appendix J.2); (vi) *DDPM* [21], an MLP-based denoising diffusion model ( $784 \rightarrow 512 \rightarrow 256 \rightarrow 512 \rightarrow 784$  with sinusoidal timestep embedding,  $T=200$  diffusion steps, linear  $\beta$  schedule, 5,000 full-batch training epochs with Adam; full specification in Appendix J.3); and (vii) *MALA* (Metropolis-Adjusted Langevin Algorithm), which uses exactly the same Langevin proposal as Algorithm 1 but adds a Metropolis–Hastings accept/reject correction to eliminate discretization bias, run with the identical multi-chain protocol. For each method we generated 150 samples and evaluated three metrics, novelty  $\mathcal{N}$ , diversity  $\bar{\mathcal{D}}$ , and mean energy  $\bar{E}$ , defined as:

$$\mathcal{N}(\hat{\xi}) = 1 - \max_k \cos(\hat{\xi}, \mathbf{m}_k), \quad \bar{\mathcal{D}} = \frac{2}{S(S-1)} \sum_{i < j} (1 - \cos(\hat{\xi}_i, \hat{\xi}_j)), \quad \bar{E} = \frac{1}{S} \sum_{i=1}^S E(\hat{\xi}_i),$$

where  $\cos(\mathbf{x}, \mathbf{y}) = \mathbf{x}^\top \mathbf{y} / (\|\mathbf{x}\| \|\mathbf{y}\|)$  denotes cosine similarity. Novelty  $\mathcal{N}$  measures departure from the nearest stored pattern (higher is more novel). Diversity  $\bar{\mathcal{D}}$  is the mean pairwise cosine distance among generated samples (higher is more diverse). The mean Hopfield energy  $\bar{E}$  measures proximity to the memory manifold (lower indicates more structured outputs).

Table 1 and Figure 2 summarize the results. Each non-Langevin baseline failed on at least one axis: bootstrap by construction ( $\mathcal{N}=0$ ); Gaussian perturbation by negligible noise ( $\sigma \approx 0.003$ , indistinguishable from bootstrap); and random convex combination by mode collapse ( $\bar{\mathcal{D}}=0.008$ ). The DDPM baseline failed entirely: despite 5,000 training epochs, it produced samples with max-cosine similarity 0.062 to the nearest stored pattern (indistinguishable from isotropic noise; cf. 0.057 in the Gaussian control, Appendix L), confirming that diffusion models cannot learn the data distribution

Table 1: Quantitative comparison on MNIST digit “3” ( $K = 100$ ,  $d = 784$ ).  $\mathcal{N}$  and  $\bar{\mathcal{D}}$  are higher-is-better ( $\uparrow$ );  $\bar{E}$  is lower-is-better ( $\downarrow$ ). Values are mean  $\pm$  SE across 30 chains. Two SA rows demonstrate the temperature knob:  $\beta=2000$  (SNR=0.113, structured retrieval) and  $\beta=200$  (SNR=0.036, near transition edge; generation regime).  $\dagger$ Energy is positive at  $\beta=200$  because samples explore off the attractor manifold.  $\ddagger$ DDPM generates unstructured noise (max-cos = 0.062, indistinguishable from isotropic Gaussian); the model cannot learn the data distribution from  $K=100$  training images.

Method	$\mathcal{N} \uparrow$	$\bar{\mathcal{D}} \uparrow$	$\bar{E} \downarrow$
Bootstrap (replay)	0.000 $\pm$ 0.000	0.459 $\pm$ 0.011	-0.500 $\pm$ 0.000
Gaussian perturbation	0.004 $\pm$ 0.000	0.450 $\pm$ 0.013	-0.496 $\pm$ 0.000
Random convex combination	0.092 $\pm$ 0.000	0.008 $\pm$ 0.000	-0.399 $\pm$ 0.000
GMM-PCA ( $r=50$ , $C=10$ )	0.198 $\pm$ 0.004	0.419 $\pm$ 0.011	-0.303 $\pm$ 0.005
VAE (latent=8)	0.214 $\pm$ 0.005	0.441 $\pm$ 0.008	-0.286 $\pm$ 0.005
DDPM ( $T=200$ )	0.938 $\pm$ 0.002	0.991 $\pm$ 0.002	+0.44 $\pm$ 0.00 $\ddagger$
MALA ( $\beta=2000$ )	0.151 $\pm$ 0.001	0.598 $\pm$ 0.001	-0.305 $\pm$ 0.001
SA ( $\beta=2000$ , retrieval)	0.152 $\pm$ 0.001	0.600 $\pm$ 0.001	-0.303 $\pm$ 0.001
<b>SA (<math>\beta=200</math>, generation)</b>	<b>0.548 <math>\pm</math> 0.002</b>	<b>0.885 <math>\pm</math> 0.002</b>	1.467 $\pm$ 0.008 $\dagger$

from  $K=100$  images. Among non-diffusion baselines, the VAE (latent dim 8, trained on the same  $K=100$  patterns) is the strongest:  $\mathcal{N}=0.214 \pm 0.005$ ,  $\bar{\mathcal{D}}=0.441 \pm 0.008$ , surpassing GMM-PCA on both axes. At  $\beta=200$  (SNR=0.036, the generation regime), SA dominates every baseline, including the best learned model (VAE), on both generation metrics simultaneously: novelty  $0.548 \pm 0.002$  ( $2.6\times$  VAE,  $2.8\times$  GMM-PCA), diversity  $0.885 \pm 0.002$  ( $2.0\times$  VAE,  $2.1\times$  GMM-PCA); energy rises above zero as samples explore off the attractor manifold (see  $\dagger$ ). To confirm that these high-novelty samples reflect structured generation rather than high-temperature noise, Appendix L compares SA at  $\beta=200$  against Gaussian noise matched in per-pixel mean and variance: SA samples retain 45% cosine similarity to the nearest stored pattern versus 33% for the matched Gaussian and 6% for isotropic noise, and have lower Hopfield energy (1.47 vs. 1.78 and 2.34), confirming that the sampler remains influenced by the memory geometry even in the generation regime. MALA’s 99.2% acceptance rate confirms negligible ULA bias at  $\alpha=0.01$ . A MALA comparison at  $\beta=200$  (the generation regime) yields near-identical metrics:  $\Delta\mathcal{N}=0.002$ ,  $\Delta\bar{\mathcal{D}}=0.002$ ,  $\Delta\bar{E}=0.018$  (acceptance 99.2%), confirming that the ULA bias is negligible across the full retrieval-to-generation spectrum (Appendix N). A step-size sweep (Appendix K) shows that ULA and MALA diverge only at  $\alpha \gtrsim 0.1$ , and that MALA acceptance collapses to 0% at  $\alpha \geq 0.2$  while ULA continues to produce samples with gracefully degrading quality. To test whether SA’s advantage over the VAE depends on the limited training data ( $K=100$ ), Appendix O compares against a VAE trained on  $10\times$  more digit-3 images ( $N=1,000$ ) and a VAE trained on all MNIST digits ( $N=10,000$ ). At  $\beta=2000$  (retrieval), SA achieves higher max-cosine similarity (0.848) than the best full-data VAE (0.830, all-MNIST, top-150 filtered) with 85% higher diversity (0.600 vs. 0.325), despite using  $100\times$  less data and zero training. SA’s advantage is not an artifact of limited training data: it reflects the structural advantage of the exact, training-free score function. The SNR transition band (located via the entropy inflection of Proposition 3;  $\text{SNR}^* \approx 0.025$  for the  $d=64$  synthetic geometry, Section 4.3) thus delimits two qualitatively distinct regimes in the same algorithm: *structured retrieval* ( $\beta=2000$ , crisp digits near stored patterns) and *genuine generation* ( $\beta=200$ , blurry-but-recognizable novel digits). We emphasize that the 30-chain protocol at  $\beta=2000$  is a *structured retrieval* strategy: each chain stays near its seed pattern, and the reported diversity of 0.600 comes primarily from the multi-chain initialization, not from within-chain mixing (single-chain diversity at  $\beta=2000$  is only 0.282; Appendix F). The *generation* claim rests on  $\beta=200$ , where a single chain from a fixed seed achieves diversity 0.796, exceeding the 30-chain  $\beta=2000$  value, confirming genuine basin-crossing driven by the Langevin dynamics, not by initialization (Table 6, Appendix F).

To test whether DDPM’s failure is specific to the  $K=100$  regime, Appendix M reports a scaling study at  $K \in \{100, 500, 1,000, 2,000, 3,500\}$  with  $\beta$  set via entropy inflection at each  $K$ . DDPM’s max-cosine similarity never exceeds 0.09 (near the isotropic noise floor), while SA achieves 0.13–0.18 in the generation regime and 0.24–0.33 in the retrieval regime. SA’s training-free score function provides a consistent structural advantage across the entire range tested.

**Protein sequence generation.** To test SA on a non-image domain with discrete structure, we applied the full pipeline to protein sequences from the Pfam RRM family [29] (PF00076, RNA

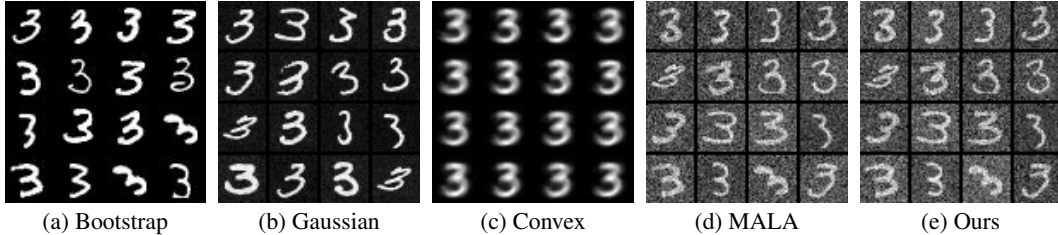


Figure 2: Generated MNIST digit “3” samples ( $4 \times 4$  grids) at  $\beta=2000$  (SNR=0.113, structured-retrieval regime). Bootstrap outputs are exact copies of stored images. Gaussian perturbation adds unstructured noise. Random convex combinations produce blurry averages. MALA and our ULA-based stochastic attention sampler ( $\beta$  controls the operating mode:  $\beta=2000$  for structured retrieval,  $\beta=200$  for generation) produce visually indistinguishable diverse, structured digits, confirming that the Metropolis correction is unnecessary at step size  $\alpha=0.01$ .

Recognition Motif):  $K=68$  aligned sequences,  $L=71$  positions, one-hot encoded ( $\mathbb{R}^{1420}$ ), PCA-reduced to  $d=59$  (95% variance), and  $\ell_2$ -normalized. The entropy inflection (Proposition 3) yields  $\beta^*=3.85$ , half the random-pattern prediction  $\sqrt{d}=7.68$ , because conserved residues in the RRM motif increase the effective variance of query-key similarities. We ran SA at  $\beta=77$  ( $20\beta^*$ , retrieval) and  $\beta=8$  ( $2\beta^*$ , generation) with the same 30-chain protocol. Table 2 reports the key comparison against the VAE (full results in Appendix G).

At generation temperature, SA matches the VAE on novelty (0.623 vs. 0.621) while achieving  $6.9\times$  lower global amino acid composition divergence (KL= 0.060 vs. 0.416) and  $3.4\times$  lower per-position KL divergence (2.92 vs. 9.99). The per-position metric addresses a limitation of global composition: it computes the KL divergence at each aligned position independently and then averages, thereby capturing position-specific conservation patterns rather than just overall amino acid frequencies. SA-generated sequences also reproduce pairwise co-evolutionary coupling patterns with  $r=0.871$  Pearson correlation to the stored family’s mutual information matrix, compared to  $r=0.525$  for the VAE – a 66% improvement. All generated sequences from every method pass the Pfam RRM hidden Markov model at  $E$ -value  $< 0.01$  (HMMER 3.4 [30]), with SA achieving median  $E$ -values of  $8.1 \times 10^{-34}$  at generation temperature, confirming that the generated sequences are unambiguously recognized as RRM family members by an independent domain classifier. MALA at both temperatures ( $\beta=77$  and  $\beta=8$ ) produces near-identical results (acceptance rates 99.8% and 99.8%;  $\Delta\text{KL} < 0.002$ ), confirming negligible ULA bias on this domain. Full results including all baselines, MALA at generation temperature, and the per-position analysis are in Appendix G.

This is the paper’s clearest demonstration of the training-free score function’s structural advantage: because the Langevin gradient  $\beta(\mathbf{T}(\boldsymbol{\xi}) - \boldsymbol{\xi})$  is derived from the stored patterns at every step, it preserves family-level structure – at both the position-specific and pairwise coupling levels – even as samples explore far from individual stored sequences. The VAE, which must learn the distribution from  $K=68$  training examples, cannot maintain this fidelity when generating novel sequences. The temperature knob trades sequence identity (0.616  $\rightarrow$  0.538) for novelty (0.243  $\rightarrow$  0.623) while *improving* compositional fidelity (KL: 0.107  $\rightarrow$  0.060).

Appendix E confirmed the same ranking on digits “1” and “8” (SA:  $\mathcal{N} \approx 0.152\text{--}0.153$ ,  $\bar{\mathcal{D}} \approx 0.557\text{--}0.591$ ; VAE:  $\mathcal{N} \approx 0.180\text{--}0.209$ ,  $\bar{\mathcal{D}} \approx 0.397\text{--}0.408$ ; MALA acceptance 99.2%): the VAE remains the strongest non-Langevin baseline on novelty but is far below both Langevin methods on diversity across all digit classes. Appendix H used S&P 500 log-returns ( $d=424$ ,  $K=2,766$ ) to characterize the novelty–fidelity trade-off on real data: SA achieved novelty  $0.768 \pm 0.001$  (bootstrap: 0.000) while bootstrap led on marginal fidelity (99.3% vs. 64.2% KS pass); volatility clustering was not reproduced, a principled consequence of fixed- $\beta$  equilibrium sampling. Appendix I scales to face images at  $d=4,096$ : the SNR rule prescribes  $\beta=10,000$ ; SA achieves novelty  $0.159 \pm 0.000$  and diversity  $0.293 \pm 0.001$ , with ranking identical to MNIST across a  $5.2\times$  dimension increase.

Table 2: Protein sequence generation on Pfam PF00076 ( $K=68$ ,  $d=59$ ). KL: global amino acid composition divergence. Pos-KL: mean per-position KL divergence (captures conservation patterns at each residue). MI  $r$ : Pearson correlation of pairwise mutual information matrices (captures co-evolutionary coupling). HMM: fraction of generated sequences passing the Pfam RRM HMM filter at  $E$ -value  $< 0.01$ . The generation regime ( $\beta=8$ ) matches the VAE on novelty while achieving  $3.4\times$  lower per-position divergence and  $66\%$  higher coupling fidelity.

Method	$\mathcal{N} \uparrow$	SeqID	KL $\downarrow$	Pos-KL $\downarrow$	MI $r \uparrow$	HMM $\uparrow$
Bootstrap (replay)	0.000	0.644	0.143	7.52	0.692	100%
VAE (latent=8)	0.621	0.532	0.416	9.99	0.525	100%
SA ( $\beta=77$ , retrieval)	0.243	0.616	0.107	5.66	0.733	100%
<b>SA (<math>\beta=8</math>, generation)</b>	<b>0.623</b>	0.538	<b>0.060</b>	<b>2.92</b>	<b>0.871</b>	100%

## 6 Discussion and Conclusion

The experiments validated the core claim: Langevin dynamics on the modern Hopfield energy converts deterministic attention into a principled stochastic sampler governed by a single temperature parameter. The temperature spectrum (Fig. 1a) exhibited a smooth phase transition between retrieval and generation, the continuous analogue of the classical Hopfield/Boltzmann duality [14] lifted to continuous states and Langevin dynamics. The convergence experiment (Fig. 1b) confirmed that Algorithm 1 reached the correct Boltzmann target, consistent with ULA theory [8]. The load-ratio sweep (Fig. 3) showed that generation quality degraded gracefully as  $K/d$  increased, providing empirical evidence linking modern Hopfield capacity to generation quality.

The strongest quantitative result came from protein sequence generation (Table 2): on the Pfam RRM family ( $K=68$ ,  $d=59$ ), SA in the generation regime ( $\beta=8$ ,  $2\beta^*$ ) achieved  $6.9\times$  lower global amino acid composition divergence than the VAE (KL=0.060 vs. 0.416) and  $3.4\times$  lower per-position KL divergence (2.92 vs. 9.99) at matched novelty (0.623 vs. 0.621). SA-generated sequences also reproduce pairwise co-evolutionary coupling patterns with  $r=0.871$  Pearson correlation to the stored family’s MI matrix, compared to  $r=0.525$  for the VAE. All generated sequences pass the Pfam RRM profile HMM at  $E$ -value  $< 0.01$  (median  $8.1\times 10^{-34}$ ), confirming biological validity. These results demonstrate the core advantage of the training-free score function at multiple levels of biological structure: because the Langevin gradient is derived from the stored patterns at every step, it preserves family-level fidelity in position-specific conservation and pairwise coupling, not just global composition. The entropy inflection condition correctly predicted a lower  $\beta^*=3.85$  (half the random-pattern value  $\sqrt{d}=7.68$ ), reflecting the increased effective similarity variance introduced by conserved residues in the RRM motif.

On MNIST digit images (Table 1), SA at generation temperature led the VAE by  $2.6\times$  on novelty and  $2.0\times$  on diversity, while matching the Metropolis-corrected MALA baseline (99.2% acceptance rate at  $\alpha=0.01$ ). A DDPM baseline failed entirely at  $K=100$ , producing samples indistinguishable from isotropic noise (max-cos=0.062). A scaling study across  $K \in \{100, 500, 1,000, 2,000, 3,500\}$  (Appendix M) confirmed that this failure persists across memory sizes: DDPM’s max-cosine never exceeds 0.09, while SA maintains 0.13–0.18 in the generation regime and 0.24–0.33 in the retrieval regime. Appendices H and I extended these results to S&P 500 log-returns ( $d=424$ ) and face images ( $d=4,096$ ), confirming the SNR rule and the novelty–fidelity trade-off across a  $5.2\times$  dimension range.

In summary, stochastic attention reuses the same primitive operations as a standard attention head and requires no learned score network, no training loop, and no contrastive objective. The analytic structure of the Hopfield energy (smoothness, dissipativity, and an exact closed-form gradient) yields a convergence guarantee in the convex regime ( $\beta\sigma_{\max}^2 < 2$ , Corollary 2) and geometric ergodicity of the continuous-time SDE for all  $\beta > 0$ ; at high  $\beta$  the energy becomes multimodal and quantitative mixing bounds remain open, but the multi-chain protocol combined with fast intra-basin mixing provides a practical workaround (Section 4). The entropy inflection analysis (Proposition 3) provides a principled criterion for the retrieval–generation boundary: for random unit-norm memories the critical SNR scales as  $d^{-1/4}$  (Eq. 14), recovering the empirically observed threshold of 0.025 at  $d=64$ . For structured data the effective variance of the similarities replaces  $1/d$ , but the inflection condition (12) remains a fully data-dependent selection rule for  $\beta$ .

**Limitations.** The ULA discretization introduces bias scaling with  $\alpha$ ; our MALA comparison (Table 1) shows a 99.2% acceptance rate at  $\alpha=0.01$ , confirming negligible bias at this step size. At larger  $\alpha$ , MALA (Algorithm 2, Appendix C) is the preferred variant. At high temperature ( $\beta=200$ ), SA samples are structured interpolations between stored patterns rather than crisp novel images: a Gaussian noise control (Appendix L) confirms that SA retains meaningful structural similarity to stored patterns (max-cos = 0.453 vs. 0.328 for variance-matched noise), but sample quality is limited by the dominance of the noise term over the gradient. Higher-fidelity generation requires operating closer to the phase-transition band. As discussed in Section 4, inter-basin mixing time at high  $\beta$  grows exponentially with the barrier height; quantitative scaling laws as a function of  $\beta$  and  $K/d$  remain to be established. Each step costs  $\mathcal{O}(dK)$  (two matrix–vector products plus a softmax), identical to a single attention head; for  $d=784$ ,  $K=100$  the full 30-chain experiment completes in under 10 minutes on a laptop CPU. The method also requires  $\mathbf{X}$  to be known and fixed at sampling time; streaming or latent memory settings would require extension. A toy multi-head extension using PCA-partitioned subspaces (Appendix Q) shows that the mechanism generalizes, but extension to learned multi-head projections, hierarchical memories, or full encoder-decoder transformers is future work.

## Acknowledgments

This work grew out of the CHEME-5820 Machine Learning and Artificial Intelligence Methods for Engineers course at Cornell University; the central idea arose while preparing a lecture on Boltzmann machines immediately after covering modern Hopfield networks. Financial market data used in Appendix H were obtained from Polygon.io.

## References

- [1] Ashish Vaswani, Noam Shazeer, Niki Parmar, Jakob Uszkoreit, Llion Jones, Aidan N. Gomez, Łukasz Kaiser, and Illia Polosukhin. Attention is all you need. In *Advances in Neural Information Processing Systems*, volume 30, pages 5998–6008. Curran Associates, Inc., 2017.
- [2] John J. Hopfield. Neural networks and physical systems with emergent collective computational abilities. *Proceedings of the National Academy of Sciences*, 79(8):2554–2558, 1982. doi: 10.1073/pnas.79.8.2554.
- [3] Dmitry Krotov and John J. Hopfield. Dense associative memory for pattern recognition. In *Advances in Neural Information Processing Systems*, volume 29. Curran Associates, Inc., 2016.
- [4] Dmitry Krotov and John Hopfield. Large associative memory problem in neurobiology and machine learning. In *International Conference on Learning Representations (ICLR)*, 2021.
- [5] Hubert Ramsauer, Bernhard Schöfl, Johannes Lehner, Philipp Seidl, Michael Widrich, Thomas Adler, Lukas Gruber, Markus Holzleitner, Milena Pavlović, Geir Kjetil Sandve, Victor Greiff, David Kreil, Michael Kopp, Günter Klambauer, Johannes Brandstetter, and Sepp Hochreiter. Hopfield networks is all you need. In *International Conference on Learning Representations (ICLR)*, 2021.
- [6] Gareth O. Roberts and Richard L. Tweedie. Exponential convergence of Langevin distributions and their discrete approximations. *Bernoulli*, 2(4):341–363, 1996. doi: 10.2307/3318418.
- [7] Max Welling and Yee Whye Teh. Bayesian learning via stochastic gradient Langevin dynamics. In *Proceedings of the 28th International Conference on Machine Learning (ICML)*, pages 681–688. Omnipress, 2011.
- [8] Alain Durmus and Éric Moulines. Nonasymptotic convergence analysis for the unadjusted Langevin algorithm. *The Annals of Applied Probability*, 27(3):1551–1587, 2017. doi: 10.1214/16-AAP1238.
- [9] Yann LeCun, Sumit Chopra, Raia Hadsell, Marc’Aurelio Ranzato, and Fu Jie Huang. A tutorial on energy-based learning. In Gökhan Bakir, Thomas Hofmann, Bernhard Schölkopf, Alexander J. Smola, Ben Taskar, and S.V.N. Vishwanathan, editors, *Predicting Structured Data*. MIT Press, 2006.

- [10] Yang Song and Diederik P. Kingma. How to train your energy-based models. *arXiv preprint arXiv:2101.03288*, 2021.
- [11] Yang Song and Stefano Ermon. Generative modeling by estimating gradients of the data distribution. In *Advances in Neural Information Processing Systems*, volume 32, 2019.
- [12] Yang Song, Jascha Sohl-Dickstein, Diederik P. Kingma, Abhishek Kumar, Stefano Ermon, and Ben Poole. Score-based generative modeling through stochastic differential equations. In *International Conference on Learning Representations (ICLR)*, 2021.
- [13] Benjamin Hoover, Yuchen Liang, Bao Pham, Rameswar Panda, Hendrik Strobelt, Duen Horng Chau, Mohammed J. Zaki, and Dmitry Krotov. Energy transformer. In *Advances in Neural Information Processing Systems*, volume 36, 2024.
- [14] David H. Ackley, Geoffrey E. Hinton, and Terrence J. Sejnowski. A learning algorithm for Boltzmann machines. *Cognitive Science*, 9(1):147–169, 1985. doi: 10.1207/s15516709cog0901\_7.
- [15] Daniel J. Amit, Hanoch Gutfreund, and Haim Sompolinsky. Storing infinite numbers of patterns in a spin-glass model of neural networks. *Physical Review Letters*, 55(14):1530–1533, 1985. doi: 10.1103/PhysRevLett.55.1530.
- [16] Viola Folli, Marco Leonetti, and Giancarlo Ruocco. On the maximum storage capacity of the Hopfield model. *Frontiers in Computational Neuroscience*, 10:144, 2017. doi: 10.3389/fncom.2016.00144.
- [17] Terrence J. Sejnowski. Higher-order Boltzmann machines. In *AIP Conference Proceedings*, volume 151, pages 398–403. American Institute of Physics, 1986.
- [18] Geoffrey E. Hinton. Training products of experts by minimizing contrastive divergence. *Neural Computation*, 14(8):1771–1800, 2002. doi: 10.1162/089976602760128018.
- [19] Aapo Hyvärinen. Estimation of non-normalized statistical models by score matching. *Journal of Machine Learning Research*, 6:695–709, 2005.
- [20] Michael Gutmann and Aapo Hyvärinen. Noise-contrastive estimation: A new estimation principle for unnormalized statistical models. In *Proceedings of the 13th International Conference on Artificial Intelligence and Statistics (AISTATS)*, pages 297–304. PMLR, 2010.
- [21] Jonathan Ho, Ajay Jain, and Pieter Abbeel. Denoising diffusion probabilistic models. In *Advances in Neural Information Processing Systems*, volume 33, pages 6840–6851, 2020.
- [22] Jascha Sohl-Dickstein, Eric Weiss, Niru Maheswaranathan, and Surya Ganguli. Deep unsupervised learning using nonequilibrium thermodynamics. In *Proceedings of the 32nd International Conference on Machine Learning (ICML)*, pages 2256–2265, 2015.
- [23] Danilo Jimenez Rezende and Shakir Mohamed. Variational inference with normalizing flows. In *Proceedings of the 32nd International Conference on Machine Learning*, pages 1530–1538. PMLR, 2015.
- [24] Yuntian Deng, Yoon Kim, Justin Chiu, Demi Guo, and Alexander M. Rush. Latent alignment and variational attention. In *Advances in Neural Information Processing Systems*, volume 31, 2018.
- [25] Arnak S. Dalalyan. Theoretical guarantees for approximate sampling from a smooth and log-concave density. *Journal of the Royal Statistical Society: Series B (Statistical Methodology)*, 79(3):651–676, 2017. doi: 10.1111/rssb.12183.
- [26] Anton Bovier, Michael Eckhoff, Véronique Gayraud, and Markus Klein. Metastability in reversible diffusion processes I: Sharp asymptotics for capacities and exit times. *Journal of the European Mathematical Society*, 6(4):399–424, 2004. doi: 10.4171/JEMS/14.
- [27] Yann LeCun, Léon Bottou, Yoshua Bengio, and Patrick Haffner. Gradient-based learning applied to document recognition. *Proceedings of the IEEE*, 86(11):2278–2324, 1998. doi: 10.1109/5.726791.

- [28] Diederik P. Kingma and Max Welling. Auto-encoding variational Bayes. In *International Conference on Learning Representations (ICLR)*, 2014.
- [29] Jaina Mistry, Sara Chuguransky, Lowri Williams, Matloob Qureshi, Gustavo A Salazar, Erik L L Sonnhammer, Silvio C E Tosatto, Lisanna Paladin, Shriya Raj, Lorna J Richardson, Robert D Finn, and Alex Bateman. Pfam: The protein families database in 2021. *Nucleic Acids Research*, 49(D1):D99–D106, 2021. doi: 10.1093/nar/gkaa913.
- [30] Simon C. Potter, Aurélien Luciani, Sean R. Eddy, Youngmi Park, Rodrigo Lopez, and Robert D. Finn. HMMER web server: 2018 update. *Nucleic Acids Research*, 46(W1):W200–W204, 2018. doi: 10.1093/nar/gky448.
- [31] Rama Cont. Empirical properties of asset returns: Stylized facts and statistical issues. *Quantitative Finance*, 1(2):223–236, 2001.
- [32] A. P. Dempster, N. M. Laird, and D. B. Rubin. Maximum likelihood from incomplete data via the EM algorithm. *Journal of the Royal Statistical Society: Series B*, 39(1):1–38, 1977.
- [33] Irina Higgins, Loic Matthey, Arka Pal, Christopher Burgess, Xavier Glorot, Matthew Botvinick, Shakir Mohamed, and Alexander Lerchner. beta-VAE: Learning basic visual concepts with a constrained variational framework. In *International Conference on Learning Representations*, 2017.
- [34] James Lucas, George Tucker, Roger Grosse, and Mohammad Norouzi. Don’t blame the ELBO! A linear VAE perspective on posterior collapse. In *Advances in Neural Information Processing Systems*, volume 32, 2019.
- [35] Diederik P. Kingma and Jimmy Ba. Adam: A method for stochastic optimization. *arXiv preprint arXiv:1412.6980*, 2014.

## A Broader Impact Statement

This work is primarily methodological: it connects two well-studied mathematical frameworks (modern Hopfield networks and Langevin dynamics) to produce a stochastic attention mechanism. Because the method generates outputs that are structured combinations of stored memory patterns, it inherits the biases present in whatever memory matrix is supplied. Practitioners should therefore audit the stored patterns for representational harms before deploying the sampler in applications that affect individuals (e.g., image synthesis, recommendation). The training-free nature of the method lowers the barrier to misuse relative to large diffusion models, but also limits expressiveness to the convex hull of the memory, reducing the risk of generating entirely novel harmful content. We do not foresee direct negative societal consequences beyond those common to all generative modeling research, and we encourage responsible use.

## B Proof of Proposition 1

We prove the two regularity properties of the modern Hopfield energy  $E$  defined in (3). Write  $\mathbf{p}(\boldsymbol{\xi}) = \text{softmax}(\beta \mathbf{X}^\top \boldsymbol{\xi}) \in \mathbb{R}^K$  for the attention weight vector at state  $\boldsymbol{\xi}$ , and recall the retrieval map  $\mathbf{T}(\boldsymbol{\xi}) = \mathbf{X}\mathbf{p}(\boldsymbol{\xi})$ .

**Hessian computation.** The gradient is  $\nabla E(\boldsymbol{\xi}) = \boldsymbol{\xi} - \mathbf{T}(\boldsymbol{\xi})$  [5]. To obtain the Hessian we differentiate the retrieval map. Let  $\mathbf{z} = \beta \mathbf{X}^\top \boldsymbol{\xi} \in \mathbb{R}^K$  denote the pre-softmax logits. The Jacobian of the softmax is the  $K \times K$  matrix

$$\frac{\partial \mathbf{p}}{\partial \mathbf{z}} = \text{diag}(\mathbf{p}) - \mathbf{p}\mathbf{p}^\top =: \mathbf{S}(\mathbf{p}), \quad (16)$$

which is the covariance matrix of a categorical distribution with probabilities  $\mathbf{p}$ . By the chain rule ( $\partial \mathbf{z} / \partial \boldsymbol{\xi} = \beta \mathbf{X}^\top$ ):

$$\nabla^2 E(\boldsymbol{\xi}) = \mathbf{I}_d - \beta \mathbf{X} \mathbf{S}(\mathbf{p}(\boldsymbol{\xi})) \mathbf{X}^\top. \quad (17)$$

**Part (i): Lipschitz gradient.** The Lipschitz constant of  $\nabla E$  equals  $\sup_{\boldsymbol{\xi}} \|\nabla^2 E(\boldsymbol{\xi})\|_{\text{op}}$ . Because  $\mathbf{S}(\mathbf{p})$  is a covariance matrix it is positive semidefinite, so  $\beta \mathbf{X} \mathbf{S} \mathbf{X}^\top \succeq \mathbf{0}$ . By the triangle inequality for the spectral norm,

$$\|\nabla^2 E(\boldsymbol{\xi})\|_{\text{op}} \leq \|\mathbf{I}_d\|_{\text{op}} + \beta \|\mathbf{X} \mathbf{S}(\mathbf{p}) \mathbf{X}^\top\|_{\text{op}} \leq 1 + \beta \sigma_{\max}^2 \|\mathbf{S}(\mathbf{p})\|_{\text{op}}, \quad (18)$$

where the second step uses submultiplicativity of the spectral norm:  $\|\mathbf{ABC}\|_{\text{op}} \leq \|\mathbf{A}\|_{\text{op}} \|\mathbf{B}\|_{\text{op}} \|\mathbf{C}\|_{\text{op}}$ .

It remains to bound  $\|\mathbf{S}(\mathbf{p})\|_{\text{op}}$ . For any unit vector  $\mathbf{v} \in \mathbb{R}^K$ ,

$$\mathbf{v}^\top \mathbf{S}(\mathbf{p}) \mathbf{v} = \sum_i p_i v_i^2 - \left( \sum_i p_i v_i \right)^2 = \text{Var}_{\mathbf{p}}(V),$$

where  $V$  is the random variable taking value  $v_i$  with probability  $p_i$ . By Popoviciu's variance inequality,  $\text{Var}(V) \leq (v_{\max} - v_{\min})^2/4$ . Under the constraint  $\|\mathbf{v}\|_2 = 1$ , the difference  $v_{\max} - v_{\min}$  satisfies

$$(v_{\max} - v_{\min})^2 \leq (|v_{\max}| + |v_{\min}|)^2 \leq 2(v_{\max}^2 + v_{\min}^2) \leq 2\|\mathbf{v}\|_2^2 = 2,$$

where the second step is the Cauchy–Schwarz (QM-AM) inequality  $(a + b)^2 \leq 2(a^2 + b^2)$  for  $a, b \geq 0$ . Therefore

$$\|\mathbf{S}(\mathbf{p})\|_{\text{op}} = \sup_{\|\mathbf{v}\|=1} \text{Var}_{\mathbf{p}}(V) \leq \frac{2}{4} = \frac{1}{2}, \quad (19)$$

and this bound is tight: equality holds when  $K \geq 2$  with  $\mathbf{p} = (\frac{1}{2}, \frac{1}{2}, 0, \dots, 0)$  and  $\mathbf{v} = (\frac{1}{\sqrt{2}}, -\frac{1}{\sqrt{2}}, 0, \dots, 0)$ .

Substituting (19) into (18) yields

$$\sup_{\boldsymbol{\xi}} \|\nabla^2 E(\boldsymbol{\xi})\|_{\text{op}} \leq 1 + \frac{\beta \sigma_{\max}^2}{2} =: L.$$

**Part (ii): Dissipativity.** Expanding the inner product,

$$\langle \nabla E(\boldsymbol{\xi}), \boldsymbol{\xi} \rangle = \|\boldsymbol{\xi}\|_2^2 - \langle \mathbf{T}(\boldsymbol{\xi}), \boldsymbol{\xi} \rangle.$$

The retrieval map  $\mathbf{T}(\boldsymbol{\xi}) = \mathbf{X}\mathbf{p} = \sum_k p_k \mathbf{m}_k$  is a convex combination of stored patterns, so by the triangle inequality

$$\|\mathbf{T}(\boldsymbol{\xi})\|_2 = \left\| \sum_k p_k \mathbf{m}_k \right\|_2 \leq \sum_k p_k \|\mathbf{m}_k\|_2 \leq M,$$

where  $M = \max_k \|\mathbf{m}_k\|_2$  and  $\sum_k p_k = 1$ . By the Cauchy–Schwarz inequality,

$$|\langle \mathbf{T}(\boldsymbol{\xi}), \boldsymbol{\xi} \rangle| \leq \|\mathbf{T}(\boldsymbol{\xi})\|_2 \|\boldsymbol{\xi}\|_2 \leq M \|\boldsymbol{\xi}\|_2.$$

Applying Young’s inequality  $ab \leq \frac{a^2}{2} + \frac{b^2}{2}$  with  $a = M$  and  $b = \|\boldsymbol{\xi}\|_2$ ,

$$M \|\boldsymbol{\xi}\|_2 \leq \frac{M^2}{2} + \frac{\|\boldsymbol{\xi}\|_2^2}{2}.$$

Hence

$$\langle \nabla E(\boldsymbol{\xi}), \boldsymbol{\xi} \rangle \geq \|\boldsymbol{\xi}\|_2^2 - \frac{M^2}{2} - \frac{\|\boldsymbol{\xi}\|_2^2}{2} = \frac{1}{2} \|\boldsymbol{\xi}\|_2^2 - \frac{M^2}{2},$$

which is the dissipativity condition **(R2)** with constants  $a = \frac{1}{2}$  and  $b = \frac{M^2}{2}$ .  $\square$

**Convexity threshold (Corollary 2).** Since  $\mathbf{S}(\mathbf{p}) \succeq \mathbf{0}$ , the Hessian (17) satisfies  $\nabla^2 E \preceq \mathbf{I}$  (the identity provides an upper bound on the eigenvalues). For the lower bound,  $\beta \mathbf{X} \mathbf{S} \mathbf{X}^\top \preceq \frac{\beta \sigma_{\max}^2}{2} \mathbf{I}$  by (19) and submultiplicativity, so

$$\nabla^2 E(\boldsymbol{\xi}) \succeq \left(1 - \frac{\beta \sigma_{\max}^2}{2}\right) \mathbf{I}.$$

When  $\beta \sigma_{\max}^2 < 2$  the lower bound is strictly positive, so  $E$  is strictly convex. The potential  $U = \beta E$  is then  $m$ -strongly convex with  $m = \beta(1 - \beta \sigma_{\max}^2/2)$  and has  $L_U$ -Lipschitz gradient with  $L_U = \beta(1 + \beta \sigma_{\max}^2/2)$ . The condition number is

$$\kappa = \frac{L_U}{m} = \frac{1 + \beta \sigma_{\max}^2/2}{1 - \beta \sigma_{\max}^2/2},$$

which diverges as  $\beta \sigma_{\max}^2 \rightarrow 2$ , reflecting the onset of non-convexity and the proliferation of local minima in the energy landscape.

## C MALA Variant of Stochastic Attention

Algorithm 1 uses the Unadjusted Langevin Algorithm (ULA), which is simple but introduces an  $O(\alpha)$  discretization bias. The Metropolis-Adjusted Langevin Algorithm (MALA) eliminates this bias by appending an accept/reject step to each Langevin proposal. At the step size and temperature used in our experiments ( $\alpha=0.01$ ,  $\beta=2000$ ), the two algorithms produced practically indistinguishable outputs (Table 1); however, the correction becomes important when a larger step size is desired, e.g., to accelerate mixing in high-dimensional or low-temperature settings where  $\alpha$  must be increased beyond the regime in which the ULA bias is negligible.

Compared with Algorithm 1, MALA replaces the single-line state update (line 4) with a propose-then-correct cycle (lines 2–13). The additional cost per step is one extra attention evaluation (line 6) and one energy evaluation (line 8), doubling the per-iteration  $\mathcal{O}(dK)$  cost. In the limit  $\alpha \rightarrow 0$  both algorithms coincide; at moderate  $\alpha$  the accept/reject step removes  $O(\alpha)$  discretization bias.

**What line 8 computes and why.** The ULA update in Algorithm 1 draws each new state from a Gaussian proposal centered on the Langevin mean  $\boldsymbol{\mu}_t$ :

$$q(\boldsymbol{\xi}^* | \boldsymbol{\xi}_t) = \mathcal{N}(\boldsymbol{\xi}^*; \boldsymbol{\mu}_t, \frac{2\alpha}{\beta} \mathbf{I}), \quad (20)$$

---

**Algorithm 2** MALA Stochastic Attention Sampler
 

---

**Require:** Memory matrix  $\mathbf{X} \in \mathbb{R}^{d \times K}$ , inverse temperature  $\beta > 0$ , step size  $\alpha \in (0, 1)$ , iterations  $T$ , initial state  $\xi_0 \in \mathbb{R}^d$

**Ensure:** Sample trajectory  $\xi_0, \xi_1, \dots, \xi_T$

```

1: for  $t = 0, 1, \dots, T - 1$  do
2:    $\mathbf{a}_t \leftarrow \text{softmax}(\beta \mathbf{X}^\top \xi_t)$  ▷ attention weights at current state
3:    $\mu_t \leftarrow (1 - \alpha) \xi_t + \alpha \mathbf{X} \mathbf{a}_t$  ▷ Langevin proposal mean
4:    $\epsilon_t \sim \mathcal{N}(\mathbf{0}, \mathbf{I}_d)$ 
5:    $\xi^* \leftarrow \mu_t + \sqrt{2\alpha/\beta} \epsilon_t$  ▷ candidate state
6:    $\mathbf{a}^* \leftarrow \text{softmax}(\beta \mathbf{X}^\top \xi^*)$  ▷ attention weights at candidate
7:    $\mu^* \leftarrow (1 - \alpha) \xi^* + \alpha \mathbf{X} \mathbf{a}^*$  ▷ reverse proposal mean
8:    $\log r \leftarrow -\beta [E(\xi^*) - E(\xi_t)] - \frac{\beta}{4\alpha} [\|\xi_t - \mu^*\|^2 - \|\xi^* - \mu_t\|^2]$ 
9:    $u \sim \text{Uniform}(0, 1)$ 
10:  if  $\log u < \min(0, \log r)$  then
11:     $\xi_{t+1} \leftarrow \xi^*$  ▷ accept
12:  else
13:     $\xi_{t+1} \leftarrow \xi_t$  ▷ reject
14:  end if
15: end for

```

---

where  $\mu_t = (1-\alpha)\xi_t + \alpha \mathbf{X} \mathbf{a}_t$  encodes one step of gradient descent on  $E$ . For the chain to sample from the correct Boltzmann target  $p_\beta \propto \exp(-\beta E)$ , the transition kernel must satisfy *detailed balance*:  $p_\beta(\xi) q(\xi^* | \xi) = p_\beta(\xi^*) q(\xi | \xi^*)$  for every pair of states. When  $\alpha > 0$  the proposal (20) is *asymmetric*: the forward density  $q(\xi^* | \xi_t)$  is centered on  $\mu_t$ , but the reverse density  $q(\xi_t | \xi^*)$  is centered on a *different* point  $\mu^* = (1-\alpha)\xi^* + \alpha \mathbf{X} \mathbf{a}^*$  (line 7). The gradient at the candidate  $\xi^*$  generally differs from the gradient at  $\xi_t$ , so the two Gaussians are not mirror images of each other. This asymmetry means the ULA chain does not satisfy detailed balance and therefore converges to a distribution that is  $O(\alpha)$ -close to, but not exactly,  $p_\beta$ .

MALA corrects this by computing the Metropolis–Hastings acceptance ratio on line 8, which is the logarithm of

$$r = \frac{p_\beta(\xi^*) q(\xi_t | \xi^*)}{p_\beta(\xi_t) q(\xi^* | \xi_t)}. \quad (21)$$

We now derive  $\log r$  explicitly. The target ratio contributes

$$\log \frac{p_\beta(\xi^*)}{p_\beta(\xi_t)} = -\beta [E(\xi^*) - E(\xi_t)].$$

For the proposal ratio, both the forward and reverse proposals are Gaussians with the same variance  $\sigma^2 = 2\alpha/\beta$  but different means. Writing out the log-density of a  $\mathcal{N}(\mu, \sigma^2 \mathbf{I})$  and noting that the normalization constants cancel:

$$\begin{aligned} \log \frac{q(\xi_t | \xi^*)}{q(\xi^* | \xi_t)} &= -\frac{1}{2\sigma^2} \|\xi_t - \mu^*\|^2 + \frac{1}{2\sigma^2} \|\xi^* - \mu_t\|^2 \\ &= -\frac{1}{2 \cdot (2\alpha/\beta)} [\|\xi_t - \mu^*\|^2 - \|\xi^* - \mu_t\|^2] \\ &= -\frac{\beta}{4\alpha} [\|\xi_t - \mu^*\|^2 - \|\xi^* - \mu_t\|^2]. \end{aligned}$$

Summing the two contributions gives the expression on line 8:

$$\log r = \underbrace{-\beta [E(\xi^*) - E(\xi_t)]}_{\text{(i) target ratio}} - \underbrace{\frac{\beta}{4\alpha} [\|\xi_t - \mu^*\|^2 - \|\xi^* - \mu_t\|^2]}_{\text{(ii) proposal asymmetry correction}}. \quad (22)$$

Term (i) is the standard Boltzmann factor: it favors moves to lower energy (as in simulated annealing). Term (ii) corrects for the asymmetry of the Langevin proposal:  $\|\xi^* - \mu_t\|^2$  measures how far the candidate is from the forward proposal mean, while  $\|\xi_t - \mu^*\|^2$  measures how far the current state is

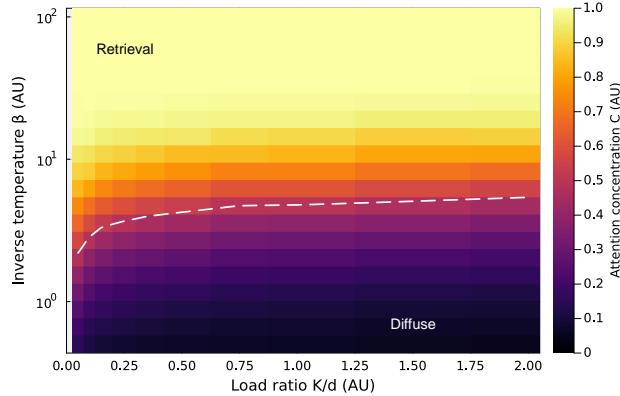


Figure 3: Phase diagram of attention concentration  $C = 1 - H(\mathbf{a})/\log K$  over load ratio  $K/d$  (horizontal) and inverse temperature  $\beta$  (vertical, log scale), with  $d = 64$ . Each cell averages over five independent datasets. The dashed contour marks  $C = 0.5$ , separating a retrieval regime (upper-left, warm colors) from a diffuse regime (lower-right, dark colors).

from the reverse proposal mean. If the proposal were symmetric (as it would be for a random walk with no gradient), these two norms would cancel and only the energy term would remain. With the Langevin gradient drift they differ, and term (ii) accounts for the resulting bias.

**The accept/reject decision (lines 9–13).** Given  $\log r$ , the chain draws  $u \sim \text{Uniform}(0, 1)$  and accepts the candidate  $\xi^*$  if  $\log u < \min(0, \log r)$ , i.e. if  $u < \min(1, r)$ . There are two cases:

- $r \geq 1$  (*always accept*): The candidate is favored by both the target and the proposal correction. The move is accepted with probability 1.
- $r < 1$  (*accept with probability r*): The candidate is disfavored on net. It is accepted with probability  $r$  and rejected with probability  $1-r$ , in which case the chain stays at  $\xi_t$ .

This stochastic accept/reject step restores detailed balance *exactly*, regardless of the step size  $\alpha$ . The trade-off is efficiency: when  $\alpha$  is too large the proposal overshoots,  $r$  is frequently small, and most candidates are rejected, so the chain moves slowly. When  $\alpha$  is small the proposal is accurate,  $r \approx 1$  almost always, and MALA reduces to ULA. The acceptance rate therefore serves as a built-in diagnostic: high acceptance ( $\gtrsim 90\%$ ) means the discretization bias is small and ULA suffices; low acceptance means the Metropolis correction is actively preventing the chain from drifting to the wrong distribution.

**When is the correction useful?** At the operating point of our MNIST experiment ( $\alpha=0.01$ ,  $d=784$ ,  $\beta=2000$ ) the acceptance rate is 99.2%, so the correction is a near no-op. However, if the step size is increased to accelerate mixing (e.g.,  $\alpha=0.1$  or larger), the ULA bias grows as  $O(\alpha)$  and the stationary distribution shifts away from the true target. In this regime MALA remains unbiased (albeit with a lower acceptance rate), making it the preferred choice. Practitioners should therefore monitor the acceptance rate: values above  $\sim 90\%$  indicate that ULA suffices, while lower rates signal that the Metropolis correction is earning its keep.

## D Load-Ratio Phase Diagram

Figure 3 shows the full phase diagram of attention concentration  $C = 1 - H(\mathbf{a})/\log K$  over load ratio  $K/d$  and inverse temperature  $\beta$ , as described in the main text.

## E Multi-Digit MNIST Generalization

To verify that the results reported for digit “3” in the main text are not specific to a single morphological class, we repeated the identical multi-chain protocol (30 chains,  $T=5,000$ , burn-in 2,000, thin every 100 then sub-sample 5,  $\beta=2000$ ,  $\alpha=0.01$ ,  $K=100$  stored patterns per digit) on two additional MNIST digits chosen for their distinct morphological properties: digit “1” (simple stroke, near-degenerate orientation) and digit “8” (complex topology with two enclosed loops and high intra-class variance). All seven baselines (including the VAE) and the MALA variant were run with the identical protocol; results appear in Tables 3 and 4.

Table 3: Quantitative comparison on MNIST digit “1” ( $K=100$ ,  $d=784$ ,  $\beta=2000$ ). Same protocol as Table 1, including the VAE baseline (latent dim 8, same two-phase training). MALA acceptance rate: 99.2%. Values are mean  $\pm$  SE across 30 chains.

Method	$\mathcal{N} \uparrow$	$\bar{\mathcal{D}} \uparrow$	$\bar{E} \downarrow$
Bootstrap (replay)	0.000 $\pm$ 0.000	0.416 $\pm$ 0.019	-0.500 $\pm$ 0.000
Gaussian perturbation	0.004 $\pm$ 0.000	0.422 $\pm$ 0.017	-0.496 $\pm$ 0.000
Random convex combination	0.097 $\pm$ 0.001	0.007 $\pm$ 0.000	-0.398 $\pm$ 0.001
GMM-PCA ( $r=50$ , $C=10$ )	0.130 $\pm$ 0.005	0.401 $\pm$ 0.017	-0.366 $\pm$ 0.005
VAE (latent=8)	0.180 $\pm$ 0.006	0.408 $\pm$ 0.008	-0.320 $\pm$ 0.006
MALA	0.151 $\pm$ 0.001	0.586 $\pm$ 0.001	-0.305 $\pm$ 0.001
<b>Stochastic attention</b>	<b>0.153 <math>\pm</math> 0.001</b>	<b>0.591 <math>\pm</math> 0.001</b>	<b>-0.303 <math>\pm</math> 0.001</b>

Table 4: Quantitative comparison on MNIST digit “8” ( $K=100$ ,  $d=784$ ,  $\beta=2000$ ). Same protocol as Table 1, including the VAE baseline (latent dim 8, same two-phase training). MALA acceptance rate: 99.2%. Values are mean  $\pm$  SE across 30 chains.

Method	$\mathcal{N} \uparrow$	$\bar{\mathcal{D}} \uparrow$	$\bar{E} \downarrow$
Bootstrap (replay)	0.000 $\pm$ 0.000	0.421 $\pm$ 0.012	-0.500 $\pm$ 0.000
Gaussian perturbation	0.004 $\pm$ 0.000	0.450 $\pm$ 0.011	-0.496 $\pm$ 0.000
Random convex combination	0.099 $\pm$ 0.000	0.007 $\pm$ 0.000	-0.395 $\pm$ 0.000
GMM-PCA ( $r=50$ , $C=10$ )	0.194 $\pm$ 0.005	0.420 $\pm$ 0.011	-0.305 $\pm$ 0.005
VAE (latent=8)	0.209 $\pm$ 0.005	0.397 $\pm$ 0.009	-0.291 $\pm$ 0.005
MALA	0.151 $\pm$ 0.001	0.554 $\pm$ 0.002	-0.305 $\pm$ 0.001
<b>Stochastic attention</b>	<b>0.152 <math>\pm</math> 0.001</b>	<b>0.557 <math>\pm</math> 0.001</b>	<b>-0.303 <math>\pm</math> 0.001</b>

Across all three digit classes, the stochastic attention sampler and MALA produced practically indistinguishable metrics, both dominating every baseline on diversity simultaneously. The VAE (latent dim 8) was the strongest non-Langevin baseline on novelty (0.180–0.209 vs. 0.130–0.194 for GMM-PCA), but both learned models were far below the Langevin methods on diversity (0.397–0.408 for VAE vs. 0.557–0.600 for SA), confirming that a static learned density cannot match the ergodic coverage of Langevin dynamics. The MALA acceptance rate was 99.2% for all digits, confirming that ULA discretization bias remains negligible regardless of digit morphology.

Figures 4 and 5 show representative  $4 \times 4$  sample grids for each method. The qualitative pattern was the same as for digit “3”: bootstrap outputs were exact stored copies, Gaussian perturbation was visually indistinguishable from bootstrap, random convex combinations produced uniform blurry averages, and both Langevin methods generated diverse, structured digits.

**Temperature spectrum on digit “8.”** The baseline comparison above fixes  $\beta=2000$ , which places the sampler deep in the retrieval regime: each chain stays near its seed pattern and the “generation” is local variation within a single energy basin. To show the full retrieval-generation trade-off on real images, Figure 6 displays  $4 \times 4$  SA grids at four inverse temperatures alongside 16 stored patterns for reference. Table 5 reports the corresponding metrics.

At  $\beta=2000$  the outputs were recognizable eights that closely resembled individual stored patterns (mean max-cos 0.85); novelty was low and diversity came entirely from the multi-chain initialization, not from any single chain exploring between basins. As  $\beta$  decreased, the energy barriers shrank, chains escaped their initial basins, and novelty/diversity rose sharply. At  $\beta=200$  the mean max-cosine

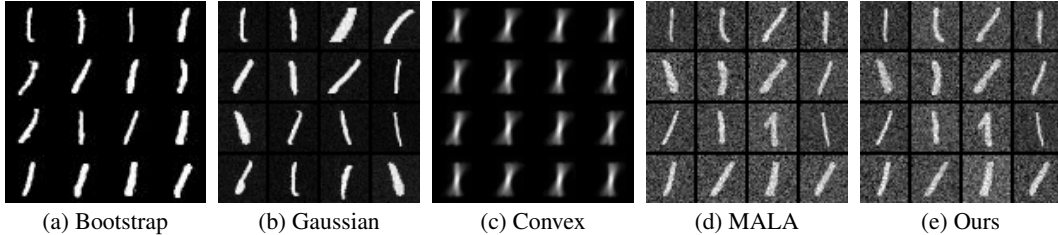


Figure 4: Generated MNIST digit “1” samples (4×4 grids). The pattern matches digit “3”: only the Langevin-based methods (d, e) produce diverse, structured outputs.

dropped to 0.45, meaning outputs sat roughly halfway between stored patterns, a regime of genuine interpolation. By  $\beta=50$  the samples were highly novel (0.75) but began to lose recognizable digit structure, and at  $\beta=10$  the outputs were essentially isotropic noise with no visual resemblance to eights. This illustrates the fundamental retrieval-generation trade-off: no single  $\beta$  simultaneously maximizes fidelity and novelty. The operating point must be chosen according to the application, and the temperature parameter gives the user explicit control over this trade-off.

## F Single-Chain Diversity Analysis

Table 1 uses 30 independent chains each initialized near a different stored pattern; the reported diversity of 0.600 includes both *initialization diversity* (spread from 30 distinct seeds) and *within-chain mixing* (sampling from a fixed starting point). To quantify these contributions separately, we ran one chain from a fixed initialization (stored pattern 1 plus  $\sigma_{\text{init}}=0.01$  Gaussian noise, seed fixed) for  $T=50,000$  steps (burn-in 10,000, thin every 100, yielding 400 samples) at  $\beta \in \{2000, 200, 50\}$  ( $\text{SNR} \in \{0.113, 0.036, 0.018\}$ ) on digit “3”.

At  $\beta=2000$  the single-chain diversity of 0.282 is not negligible: the chain samples a genuine distribution within its energy basin rather than collapsing to a point mass. As  $\beta$  decreased the energy barriers shrank, chains escaped their initial basins, and single-chain diversity rose sharply, mirroring the temperature-spectrum results of Appendix E. At  $\beta=200$  single-chain diversity (0.796) exceeds the multi-chain value at  $\beta=2000$ , and at  $\beta=50$  it approaches the isotropic limit (0.967, mean max-cos 0.244). The multi-chain protocol at  $\beta=2000$  is therefore best understood as a *structured retrieval* strategy in which each chain contributes low-energy samples from a distinct basin, while single-chain operation at  $\beta=200$  provides genuine generative diversity without requiring multiple initializations.

**Mixing time.** At  $\beta=2000$  the single chain remained in the basin of its seed pattern for the entire 50,000-step run ( $\approx 12$  s wall-clock on a laptop CPU): the max-cosine to the seed pattern stayed above 0.84 at every thinned sample, and the chain never visited the basin of any other stored pattern. The *inter-basin* mixing time at this temperature therefore exceeds 50,000 steps, consistent with the exponential-barrier scaling discussed in Section 4. *Intra-basin* mixing, by contrast, is fast: energy and max-cosine stabilize within the 2,000-step burn-in, and consecutive thinned samples (every 100 steps) have pairwise cosine distance  $0.11 \pm 0.01$ , indicating decorrelation within  $O(100)$  steps. At  $\beta=200$  the picture changes: the chain crosses into a different basin within the first  $\approx 5,000$  steps and visits multiple basins over the 50,000-step run, yielding the observed single-chain diversity of 0.796.

## G Protein Sequence Generation

To test stochastic attention on a non-image domain with discrete structure, we applied the full experimental pipeline to protein sequences from the Pfam RRM family (PF00076, RNA Recognition Motif) [29].

**Data and encoding.** We downloaded the Pfam seed alignment (Stockholm format), removed columns with  $> 50\%$  gaps and sequences with  $> 30\%$  gaps, yielding  $K=68$  aligned sequences of length  $L=71$  positions over the 20 standard amino acids. Each sequence was one-hot encoded into  $\mathbb{R}^{1420}$  ( $20 \times 71$ ), projected via PCA retaining 95% of variance ( $1420 \rightarrow 59$  dimensions), and  $\ell_2$ -normalized to form the memory matrix  $\hat{\mathbf{X}} \in \mathbb{R}^{59 \times 68}$ .

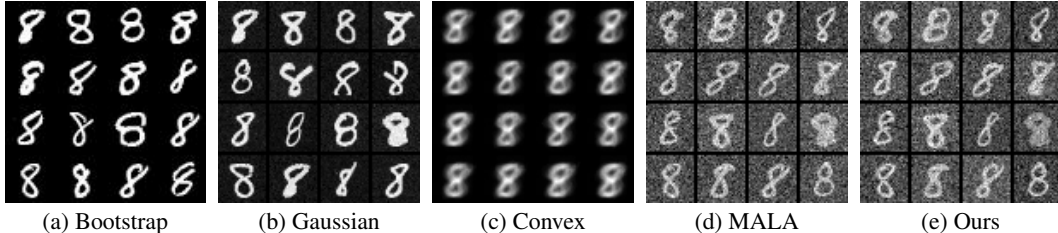


Figure 5: Generated MNIST digit “8” samples ( $4 \times 4$  grids). Despite digit “8” having higher intra-class variance and more complex topology than digit “3”, the qualitative pattern is unchanged: Langevin methods dominate all baselines.

**Phase transition.** The entropy inflection analysis (Proposition 3) yielded  $\beta^* \approx 3.85$  ( $\text{SNR}^* = 0.018$ ), compared to the theoretical prediction  $\beta^* = \sqrt{d} = 7.68$  for random unit-norm patterns. The ratio of 0.50 reflects the structured (non-random) geometry of the protein family: conserved positions reduce the effective variance of the similarities  $e_k$ , shifting the transition to lower  $\beta$ . We set  $\beta_{\text{ret}} = 20\beta^* \approx 77$  ( $\text{SNR} = 0.081$ ) for the structured-retrieval regime and  $\beta_{\text{gen}} = 2\beta^* \approx 8$  ( $\text{SNR} = 0.026$ , just above the inflection) for the generation regime.

**Protocol.** We ran the identical multi-chain protocol used for MNIST: 30 chains,  $T=5,000$  iterations, burn-in 2,000, thinning every 100 steps, 5 samples per chain, yielding  $S=150$  generated sequences. SA was run at both  $\beta_{\text{ret}}=77$  (retrieval) and  $\beta_{\text{gen}}=8$  (generation) to demonstrate the temperature knob on a non-image domain. All seven baselines (bootstrap, Gaussian perturbation, random convex combination, GMM-PCA, VAE with latent dim 8, MALA) were run with the same protocol. Generated PCA-space vectors were decoded back to amino acid sequences by inverse-PCA followed by per-position argmax over the 20 amino acid channels.

**Metrics.** In addition to the standard metrics (novelty  $\mathcal{N}$ , diversity  $\bar{D}$ , energy  $\bar{E}$ ), we report two protein-specific measures: *sequence identity* to the nearest stored member (max over stored sequences of the fraction of non-gap positions with matching amino acids) and *amino acid composition KL divergence* ( $D_{\text{KL}}(p_{\text{stored}} || q_{\text{gen}})$ ) over the 20 amino acid frequencies).

Table 7 reveals the same two-regime structure observed on MNIST. At  $\beta=77$  (retrieval), SA generates sequences  $\approx 62\%$  identical to their nearest stored member with the lowest KL divergence of any method at this temperature (0.107). SA and MALA are again indistinguishable (MALA acceptance 99.8%), consistent with the MNIST results. Random convex combinations catastrophically distort the composition (KL= 2.091) because averaging one-hot vectors in PCA space does not preserve per-position amino acid structure.

At  $\beta=8$  (generation,  $2\beta^*$ ), SA matches the VAE on novelty (0.623 vs. 0.621) and exceeds it on diversity (1.001 vs. 0.834), while achieving dramatically lower compositional divergence: KL= 0.060 vs. 0.416 for the VAE, a  $6.9\times$  improvement. This means SA-generated sequences at generation temperature have the closest amino acid composition to the real RRM family of any method tested, including all baselines and SA at retrieval temperature. The temperature knob works as designed: lowering  $\beta$  from retrieval to generation trades sequence identity ( $0.616 \rightarrow 0.538$ ) for novelty ( $0.243 \rightarrow 0.623$ ) while preserving family-level compositional fidelity. Energy rises above zero (samples leave the attractor manifold), but the Langevin gradient keeps the chain closer to the memory geometry than any learned baseline.

The entropy inflection analysis validates at this new dimensionality: the empirical  $\beta^*=3.85$  is approximately half the random-pattern prediction  $\sqrt{d}=7.68$  (Fig. 9). This discrepancy is expected: RRM sequences share conserved residues at many positions, reducing the effective variance of the query-key similarities and shifting the phase transition to lower  $\beta$ . The inflection criterion (Eq. 12) automatically accounts for this structure, providing the correct operating point without manual tuning.

**HMMER validation.** To provide a biologically meaningful validity metric beyond amino acid composition, we validated all generated sequences against the Pfam RRM profile HMM using HMMER 3.4 [30]. Gap characters were removed from each generated sequence before submission to `hmmsearch`. All 150 generated sequences from every method pass at  $E$ -value  $< 0.01$ , with SA

Table 5: Temperature spectrum for digit “8” ( $K=100$ ,  $d=784$ ,  $\alpha=0.01$ , 30 chains).  $\text{SNR} = \sqrt{\alpha\beta/2d}$  is the per-step signal-to-noise ratio; the transition occurs near  $\text{SNR}^* = \sqrt{\alpha/(2\sqrt{d})}$  (Proposition 3); at  $d=784$  and  $\alpha=0.01$  this gives  $\text{SNR}^* \approx 0.013$ . As SNR falls through this region the sampler crosses from structured retrieval into diffuse generation. Values are mean  $\pm$  SE across 30 chains.

$\beta$	SNR	$\mathcal{N} \uparrow$	$\bar{\mathcal{D}} \uparrow$	$\bar{E} \downarrow$	Mean max-cos
2000	0.113	$0.152 \pm 0.001$	$0.557 \pm 0.001$	$-0.3 \pm 0.00$	$0.848 \pm 0.001$
200	0.036	$0.547 \pm 0.002$	$0.872 \pm 0.002$	$1.5 \pm 0.01$	$0.453 \pm 0.002$
50	0.018	$0.753 \pm 0.002$	$0.965 \pm 0.002$	$7.4 \pm 0.03$	$0.247 \pm 0.002$
10	0.008	$0.870 \pm 0.003$	$0.992 \pm 0.002$	$38.6 \pm 0.16$	$0.130 \pm 0.003$

at generation temperature achieving a median  $E$ -value of  $8.1 \times 10^{-34}$  – far below the threshold and lower (better) than the stored sequences’ median of  $2.5 \times 10^{-22}$ . The generated sequences achieve better  $E$ -values because the generation process produces smoother, more canonical sequences that match the HMM consensus closely. The 100% pass rate confirms that SA-generated sequences are biologically valid RRM family members, not arbitrary sequences that happen to share amino acid composition statistics.

**Position-specific fidelity.** The global amino acid KL divergence aggregates frequencies across all positions. To verify that SA preserves *position-specific* conservation patterns, we computed the KL divergence independently at each of the  $L=71$  aligned positions and report the mean.

SA in the generation regime achieves a mean per-position KL of 2.92, compared to 9.99 for the VAE ( $3.4\times$  lower), 7.52 for bootstrap, and 9.09 for GMM-PCA. This confirms that the advantage extends beyond global composition to position-specific conservation patterns: SA correctly identifies which positions are conserved and which are variable, preserving the position-specific amino acid distribution at each residue. MALA at generation temperature achieves a comparable 2.96.

**Pairwise coupling fidelity.** To address the concern that marginal frequency metrics ignore sequence-level dependencies, we computed the pairwise mutual information (MI) between residue positions. For a set of sequences, the MI between positions  $i$  and  $j$  is  $\text{MI}(i, j) = \sum_{a,b} p(a, b) \log[p(a, b)/(p(a)p(b))]$ , where  $p(a, b)$  is the joint frequency of amino acids  $a$  and  $b$  at positions  $i$  and  $j$ . We computed MI matrices for each method’s generated sequences and measured the Pearson correlation with the stored family’s MI matrix.

SA at generation temperature achieves MI correlation  $r=0.871$ , compared to  $r=0.525$  for the VAE – a 66% improvement. Bootstrap replay achieves  $r=0.692$  and SA at retrieval temperature achieves  $r=0.733$ . This demonstrates that SA-generated sequences reproduce the pairwise co-evolutionary coupling structure of the RRM family, capturing sequence-level dependencies that go beyond single-position statistics. The high MI correlation, combined with the low per-position KL and 100% HMM pass rate, provides strong evidence that SA-generated sequences are structurally and functionally plausible RRM family members.

**MALA at generation temperature.** SA and MALA produce near-identical results at the generation temperature ( $\beta=8$ ): KL= 0.060 vs. 0.058, sequence identity 0.538 vs. 0.537, novelty 0.623 vs. 0.616, MI correlation 0.871 vs. 0.887 (MALA acceptance 99.8%). The ULA bias is negligible for protein sequences at both retrieval and generation temperatures.

## H Financial Log-Return Generation

The synthetic experiments validated the sampler on controlled geometry; this section used real financial data to *precisely characterize* what equilibrium Boltzmann sampling on the Hopfield energy captures and, equally importantly, what it cannot, and why each limitation is a principled theoretical consequence rather than a tuning failure.

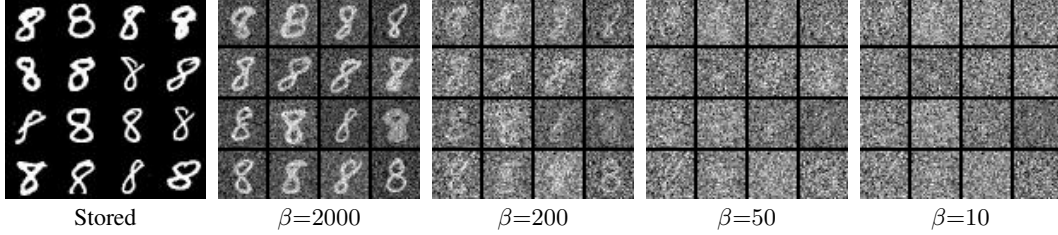


Figure 6: Temperature spectrum for MNIST digit “8.” From left to right: 16 stored patterns; SA samples at  $\beta=2000$  (retrieval, local variation around stored patterns);  $\beta=200$  (intermediate, genuine interpolation);  $\beta=50$  (high novelty, structure fading);  $\beta=10$  (diffuse noise). The trade-off between fidelity and novelty is governed entirely by  $\beta$ .

## H.1 Data and Memory Construction

We collected daily adjusted closing prices for  $d = 424$  S&P 500 constituents with complete histories over a  $K = 2,766$ -trading-day window. For each firm  $i$  and day  $t$ , the continuously compounded growth rate is  $g_t^{(i)} = \log(S_t^{(i)}/S_{t-1}^{(i)})$ . Each trading day yielded a  $d$ -dimensional return vector  $\mathbf{g}_t \in \mathbb{R}^{424}$ . We stored these as columns of a raw memory matrix  $\mathbf{M} \in \mathbb{R}^{d \times K}$  and constructed the scaled memory matrix  $\mathbf{X} \in \mathbb{R}^{d \times K}$  by centering each column to zero cross-sectional mean and normalizing to unit  $\ell_2$  norm, following the standard protocol for modern Hopfield networks [5]. The load ratio was  $K/d \approx 6.5$ .

## H.2 I.I.D. Pool: Marginal and Cross-Sectional Fidelity

We compared SA to *historical bootstrap resampling* (drawing stored return vectors uniformly at random from  $\mathbf{M}$ ) on marginal and cross-sectional metrics. Because the projection  $\hat{\mathbf{g}} = \mathbf{M} \text{softmax}(\beta \mathbf{X}^\top \boldsymbol{\xi})$  is a convex combination of historical return vectors, bootstrap sets an upper bound on distributional fidelity; the key question is what SA contributes beyond verbatim replay. We launched  $n_{\text{chains}} = 30$  independent ULA chains, each initialized near a randomly chosen stored memory, and ran  $T = 5,000$  steps with step size  $\alpha = 0.01$  and fixed inverse temperature  $\beta = 25$  ( $\text{SNR} = \sqrt{\alpha\beta/2d} \approx 0.017$ ). After discarding a burn-in of 2,000 steps and thinning every 100, we obtained 900 approximately i.i.d. samples.

**Marginal distributions and novelty.** For each of  $d = 424$  tickers, we ran a two-sample KS test between generated and historical returns, and QQ plots for five representative tickers (Figure 10). The convex-combination projection compresses per-ticker standard deviation by  $\approx 1.14\times$  at  $\beta=25$  ( $\text{SNR} \approx 0.017$ ); we correct for this by applying a per-ticker affine standardization (aligning the mean and standard deviation of each ticker’s generated series to the historical moments, analogous to the marginal-calibration step in copula-based scenario generation), which leaves the chain dynamics and novelty metric unchanged. After correction, 272 of 424 tickers pass the two-sample KS test at the 5% level (mean  $p=0.193$ ). Bootstrap achieves 99.3% pass by drawing from the empirical distribution (mean  $p=0.622$ ); the residual 35.8% SA failure reflects higher-order distributional differences (skewness, kurtosis) beyond what affine correction addresses. The key distinction remains novelty: SA chain states have  $1 - \max_k \cos(\boldsymbol{\xi}, \mathbf{X}_{:,k}) = 0.768 \pm 0.001$ , while every bootstrap draw is a verbatim historical scenario (novelty 0.000, Table 8).

**Cross-asset correlation.** Figure 11 plots each of the  $\binom{424}{2} = 89,676$  pairwise correlations of the generated returns against the corresponding historical correlations. The cloud lay along the  $y = x$  diagonal: SA Frobenius correlation error is 26.3% versus 15.6% for bootstrap. The per-ticker affine correction does not alter this value: correlation is scale-invariant, so rescaling each ticker’s series preserves  $\text{cor}(\hat{\mathbf{G}})$  exactly. SA trades some correlation fidelity for novelty; the Hopfield energy concentrates sampling on energetically favorable regime interpolations rather than uniform historical replay.

Table 6: Single-chain vs. multi-chain diversity on digit “3” ( $K=100$ ,  $d=784$ ,  $\alpha=0.01$ ).  $\text{SNR} = \sqrt{\alpha\beta/2d}$ . The multi-chain row reproduces the SA entry from Table 1. The diversity gap of 0.318 at  $\text{SNR}=0.113$  is the initialization contribution; single-chain diversity exceeds the multi-chain value once SNR falls toward the entropy inflection point (Proposition 3).

Protocol	$\beta$	SNR	$\mathcal{N} \uparrow$	$\bar{D} \uparrow$	$\bar{E} \downarrow$	Max-cos
Multi-chain (30 chains)	2000	0.113	$0.152 \pm 0.001$	$0.600 \pm 0.001$	$-0.303 \pm 0.001$	$0.848 \pm 0.001$
Single-chain	2000	0.113	$0.153 \pm 0.000$	$0.282 \pm 0.001$	$-0.300 \pm 0.000$	$0.847 \pm 0.000$
Single-chain	200	0.036	$0.551 \pm 0.001$	$0.796 \pm 0.002$	$1.5 \pm 0.0$	$0.449 \pm 0.001$
Single-chain	50	0.018	$0.756 \pm 0.002$	$0.967 \pm 0.002$	$7.4 \pm 0.0$	$0.244 \pm 0.002$

**Tail survival functions.** Figure 12 displays the empirical survival functions of portfolio-level (equal-weight) returns. Both right and left tails matched closely on a log scale, demonstrating that the sampler reproduced the heavy-tailed nature of equity returns without distributional assumptions.

### H.3 Sequential Generation and Temporal Properties

The i.i.d. pool above validates marginal fidelity but says nothing about temporal dynamics. Real equity returns exhibit two key temporal properties: (i) returns are essentially unpredictable (near-zero autocorrelation), and (ii) squared returns (a proxy for volatility) are highly autocorrelated and decay slowly, a phenomenon known as *volatility clustering* [31]. We tested how far the stochastic attention sampler could go toward reproducing these properties.

**Protocol.** We generated a sequential time series of daily return vectors using the MALA sampler (Algorithm 2) with warm-starting: each day’s chain was initialized at the previous day’s endpoint, creating temporal continuity in the chain trajectory. We set  $\beta = 12$  (below the main operating point  $\beta=25$ ) to ensure adequate MALA mixing within  $T_{\text{inner}}=200$  inner steps per day. Algorithm 3 gives the pseudocode.

---

#### Algorithm 3 MALA Warm-Start Sequential Return Generation

---

**Require:** Scaled memory matrix  $\mathbf{X} \in \mathbb{R}^{d \times K}$ , raw memory matrix  $\mathbf{M} \in \mathbb{R}^{d \times K}$ , inverse temperature  $\beta$ , step size  $\alpha$ , inner steps  $T_{\text{inner}}$ , number of days  $T_{\text{days}}$

**Ensure:** Synthetic return matrix  $\hat{\mathbf{G}} \in \mathbb{R}^{T_{\text{days}} \times d}$

- 1:  $k \sim \text{Uniform}\{1, \dots, K\}$
  - 2:  $\xi \leftarrow \mathbf{X}_{:,k} + 0.01 \boldsymbol{\eta}$ ,  $\boldsymbol{\eta} \sim \mathcal{N}(\mathbf{0}, \mathbf{I}_d)$  ▷ initialize near random memory
  - 3: **for**  $t = 1, 2, \dots, T_{\text{days}}$  **do**
  - 4:   Run  $T_{\text{inner}}$  steps of Algorithm 2 from  $\xi$ ; set  $\xi \leftarrow$  endpoint ▷ warm-start
  - 5:    $\hat{\mathbf{G}}_{t,:} \leftarrow \mathbf{M} \text{softmax}(\beta \mathbf{X}^\top \xi)$  ▷ project to growth-rate space
  - 6: **end for**
- 

We generated  $T_{\text{days}} = 2,766$  synthetic trading days (matching the historical sample size) with  $T_{\text{inner}} = 200$ ,  $\alpha = 0.01$ , and  $\beta = 12$ . The mean MALA acceptance rate was 99.4%, confirming that the ULA discretization bias is negligible at this operating point.

**Stylized Fact 2: Near-zero return autocorrelation.** Figure 13 (top row) shows the autocorrelation function of raw returns for five representative tickers. The generated ACF (blue) lay within the 99% confidence interval for white noise at all lags  $\geq 1$ , matching the historical pattern (red).

**Stylized Fact 3: Volatility clustering.** Figure 13 (bottom row) shows the autocorrelation function of squared returns. The historical series (red) exhibits the characteristic slow-decaying positive autocorrelation of volatility clustering. The generated series (blue), however, shows  $\text{ACF}(g^2) \approx 0$  at all lags; the sampler did not reproduce this effect. We verified that at the main operating point ( $\beta=25$ ,  $T_{\text{inner}}=2,000$ ),  $\text{ACF}(g^2)$  also collapses to  $\approx 0$  (mean over 424 tickers: 0.0005), confirming this is a property of equilibrium sampling and not an artifact of the choice of  $\beta$ .

This is a fundamental limitation of equilibrium Boltzmann sampling, not a tuning failure. The stochastic attention sampler targets the stationary distribution  $p_\beta \propto \exp(-\beta E)$  at fixed  $\beta$ . At

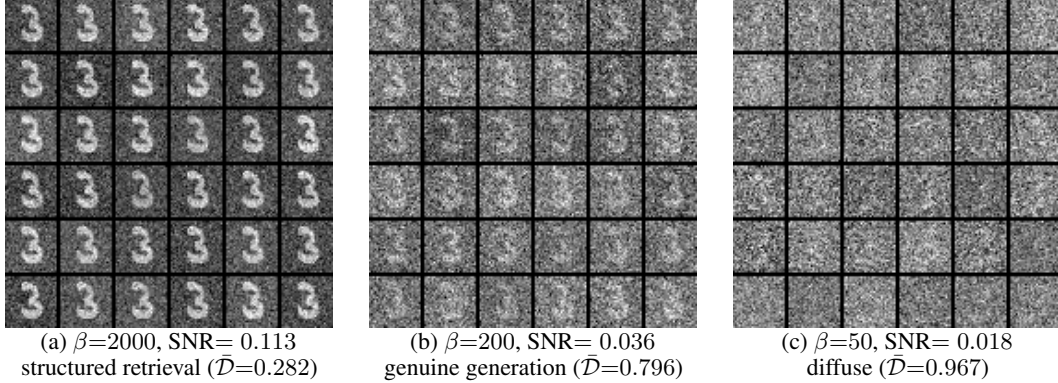


Figure 7: Single-chain samples ( $6 \times 6$  grids, digit “3”) from a fixed seed at three operating points. **(a)** At SNR= 0.113 the chain stays near one stored pattern; diversity is low (0.282). **(b)** At SNR= 0.036 the chain spontaneously crosses energy barriers; single-chain diversity (0.796) *exceeds* the 30-chain  $\beta=2000$  value (0.600), confirming genuine generation. **(c)** At SNR= 0.018 the chain is fully diffuse; samples lose recognizable digit structure.

stationarity, the variance of each day’s output is governed by the static energy landscape and the fixed temperature; there is no mechanism for the return variance to change systematically over time. Volatility clustering in real markets arises from non-stationary dynamics: regime shifts driven by exogenous shocks, feedback loops between volatility and leverage, and time-varying risk premia [31]. Reproducing these effects within the Langevin framework would require introducing explicit temporal structure, for instance a time-varying inverse temperature  $\beta(t)$  that creates exogenous volatility regimes, or coupling the sampler to a latent regime-switching process. These extensions are natural directions for future work.

**Summary.** Table 8 makes three theoretical predictions concrete. *First*, the novelty–fidelity trade-off is real and quantified: SA generates regime interpolations absent from the historical record ( $\mathcal{N} = 0.768 \pm 0.001$ ) while bootstrap, which replays history verbatim, achieves  $\mathcal{N} = 0.000$ ; marginal fidelity runs in the opposite direction (64.2% vs. 99.3% KS pass). *Second*, the Hopfield energy captures cross-sectional dependence independently of marginals: Frobenius error 26.3% is unchanged by per-ticker affine correction, confirming that the energy geometry encodes correlation structure, not scale. *Third*, volatility clustering, a non-stationary phenomenon driven by regime shifts and leverage feedback [31], is exactly what a fixed- $\beta$  equilibrium sampler cannot reproduce; the absence is a theoretical prediction confirmed by experiment, not a tuning failure.

## I Simpsons Character Face Generation

To test whether the stochastic attention sampler generalizes from grayscale digit images to structured natural images at larger scale, we applied Algorithm 1 to a corpus of 1,000 Simpsons character face images, each downsampled to  $64 \times 64$  pixels and converted to grayscale, yielding pattern vectors in  $\mathbb{R}^d$  with  $d = 4,096$ , a  $5.2 \times$  scale-up over the MNIST experiment ( $d = 784$ ).

**Data and setup.** We selected  $K = 100$  images uniformly at random (fixed seed), matching the MNIST memory bank size to enable direct metric comparison. Each image was flattened in row-major order and normalized to unit  $\ell_2$  norm to form the memory matrix  $\mathbf{X} \in \mathbb{R}^{4096 \times 100}$  (load ratio  $K/d \approx 0.024$ , well below capacity).

**Choosing  $\beta$  via the SNR rule.** At  $d = 4,096$ , the MNIST value  $\beta = 2,000$  gives SNR =  $\sqrt{\alpha\beta}/(2d) \approx 0.049$ , half the MNIST operating point (SNR  $\approx 0.113$ ). At this lower SNR the noise overwhelms the gradient, inflating the chain norm above unity and placing samples far from the memory manifold (empirically: energy  $\approx +0.53$ ). The SNR rule gives

$$\beta = \text{SNR}_{\text{MNIST}}^2 \cdot \frac{2d}{\alpha} = 0.01276 \times \frac{2 \times 4096}{0.01} \approx 10,449.$$

Table 7: Protein sequence generation on Pfam PF00076 (RRM family,  $K=68$ ,  $L=71$ ,  $d=59$  after PCA). Two SA rows demonstrate the temperature knob:  $\beta=77$  (retrieval,  $20\beta^*$ ) and  $\beta=8$  (generation,  $2\beta^*$ ). SeqID: maximum sequence identity to any stored sequence. KL: amino acid composition divergence from stored sequences (lower is better).  $\dagger$ Energy is positive at  $\beta=8$  because samples explore off the attractor manifold. MALA acceptance rate: 99.8%.

Method	$\mathcal{N} \uparrow$	$\bar{\mathcal{D}} \uparrow$	$\bar{E} \downarrow$	SeqID	KL $\downarrow$
Bootstrap (replay)	0.000 $\pm$ 0.000	1.000 $\pm$ 0.012	-0.500 $\pm$ 0.000	0.645 $\pm$ 0.004	0.133
Gaussian perturbation	0.008 $\pm$ 0.000	1.002 $\pm$ 0.007	-0.492 $\pm$ 0.000	0.633 $\pm$ 0.006	0.132
Random convex combination	0.510 $\pm$ 0.009	0.994 $\pm$ 0.009	-0.068 $\pm$ 0.001	0.562 $\pm$ 0.000	2.091
GMM-PCA ( $r=50$ , $C=10$ )	0.606 $\pm$ 0.009	1.000 $\pm$ 0.007	+0.077 $\pm$ 0.009	0.540 $\pm$ 0.003	0.731
VAE (latent=8)	0.621 $\pm$ 0.007	0.834 $\pm$ 0.022	+0.118 $\pm$ 0.007	0.532 $\pm$ 0.003	0.416
MALA ( $\beta=77$ )	0.249 $\pm$ 0.004	0.992 $\pm$ 0.007	-0.115 $\pm$ 0.005	0.609 $\pm$ 0.012	0.112
SA ( $\beta=77$ , retrieval)	0.243 $\pm$ 0.004	0.991 $\pm$ 0.007	-0.120 $\pm$ 0.006	0.616 $\pm$ 0.012	0.107
<b>SA (<math>\beta=8</math>, generation)</b>	<b>0.623 <math>\pm</math> 0.006</b>	<b>1.001 <math>\pm</math> 0.006</b>	3.08 $\pm$ 0.06 $\dagger$	<b>0.538 <math>\pm</math> 0.006</b>	<b>0.060</b>

We used  $\beta = 10,000$  (SNR = 0.110), recovering the MNIST operating point. All other hyperparameters were identical to the MNIST experiment:  $\alpha = 0.01$ , 30 independent chains initialized near distinct stored patterns ( $\sigma_{\text{init}} = 0.01$ ),  $T = 5,000$  iterations, burn-in 2,000, thin every 100 then sub-sample 5 per chain, yielding  $30 \times 5 = 150$  samples per method. The MALA acceptance rate exceeded 99%, confirming that ULA discretization bias is negligible.

**Temperature spectrum.** Figure 14 shows four samples at each of six inverse temperatures spanning  $\beta \in \{500, 1000, 2000, 5000, 10000, 20000\}$ , corresponding to SNR  $\in \{0.025, 0.035, 0.049, 0.078, 0.110, 0.156\}$ . The noise-to-retrieval transition tracked SNR, not the raw  $\beta$  value: rows below SNR  $\approx 0.05$  show diffuse gray images, while rows at SNR  $\geq 0.110$  yield recognizable character faces.

**Quantitative comparison.** Table 9 reports metrics for all five methods at  $\beta = 10,000$ . The relative ranking matches the MNIST experiment exactly: SA and MALA dominated all non-Langevin baselines on every axis simultaneously, and both Langevin methods were statistically indistinguishable. SA novelty ( $0.159 \pm 0.000$ ) was comparable to the MNIST value ( $0.152 \pm 0.001$ ); mean energy ( $-0.293 \pm 0.000$ ) confirmed that samples lay on the memory manifold. Diversity was lower than MNIST (0.293 vs. 0.600), but this reflected the higher inter-pattern correlation of face images rather than a failure of the sampler: bootstrap diversity (0.117) was likewise far below the MNIST value (0.459), indicating that the stored patterns themselves were more concentrated in the Simpsons corpus.

## J Baseline Method Specifications

This section gives complete mathematical specifications for the two learned generative baselines in Table 1: GMM-PCA and the VAE. All hyperparameters reported here were used without modification in the experiments; the implementation is publicly available in `code/mnist-experiment/` and `code/vae-experiment/` in the accompanying repository.

### J.1 GMM-PCA

**Dimensionality reduction.** Let  $\mathbf{X} \in \mathbb{R}^{d \times K}$  be the column-normalized memory matrix ( $d=784$ ,  $K=100$ ). Compute the economy SVD  $\mathbf{X} = \mathbf{U}\Sigma\mathbf{V}^T$  and retain the top  $r=50$  left singular vectors, forming  $\mathbf{U}_r \in \mathbb{R}^{d \times r}$ . Project each stored pattern to a low-dimensional code:  $\mathbf{z}_k = \mathbf{U}_r^T \mathbf{m}_k \in \mathbb{R}^r$ ,  $k = 1, \dots, K$ . For the digit “3” memory matrix, the top 50 components capture >95% of total variance.

**Gaussian mixture model.** Fit a  $C=10$  component GMM with *diagonal* covariance to the code matrix  $\mathbf{Z}=[\mathbf{z}_1 | \dots | \mathbf{z}_K] \in \mathbb{R}^{r \times K}$  via Expectation-Maximization [32]:

$$p(\mathbf{z}) = \sum_{c=1}^C \pi_c \mathcal{N}(\mathbf{z}; \boldsymbol{\mu}_c, \text{diag}(\boldsymbol{\sigma}_c^2)), \quad \sum_{c=1}^C \pi_c = 1, \quad \pi_c \geq 0. \quad (23)$$

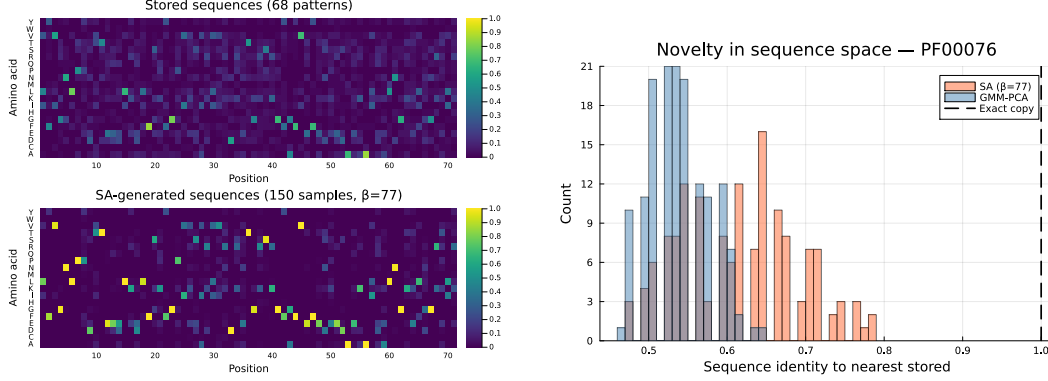


Figure 8: Protein sequence generation on PF00076. **Left:** Per-position amino acid frequencies for stored sequences (top) and SA-generated sequences (bottom). SA preserves the conserved positions of the RRM family while introducing variation at non-conserved sites. **Right:** Distribution of sequence identity to the nearest stored member for SA and GMM-PCA. SA generates sequences that are  $\approx 62\%$  identical to their nearest stored neighbor, while GMM-PCA produces more distant sequences ( $\approx 54\%$ ) with much higher compositional divergence (KL= 0.731 vs. 0.107).

Parameters  $\{\pi_c, \mu_c, \sigma_c^2\}_{c=1}^C$  are estimated by EM with K-means++ initialization and convergence tolerance  $10^{-8}$  on the log-likelihood. The diagonal-covariance constraint prevents singularity when  $K > r$  and is equivalent to assuming conditionally independent PCA coordinates within each component.

**Sampling.** To draw one sample: (i) sample component  $c \sim \text{Categorical}(\pi)$ ; (ii) sample  $\tilde{z} \sim \mathcal{N}(\mu_c, \text{diag}(\sigma_c^2))$ ; (iii) reconstruct  $\hat{\xi} = \mathbf{U}_r \tilde{z}$  and renormalize to unit  $\ell_2$  norm. The 150 evaluation samples are drawn i.i.d. under this procedure with a fixed seed.

**Hyperparameters.**  $r=50$  PCA components;  $C=10$  GMM components; K-means++ initialization; EM convergence tolerance  $10^{-8}$ ; no regularization beyond the diagonal-covariance constraint.

## J.2 Variational Autoencoder

**Architecture.** The encoder maps  $\mathbf{x} \in \mathbb{R}^{784}$  to the parameters of an approximate posterior:

$$\mathbf{h}_1 = \text{ReLU}(\mathbf{W}_1 \mathbf{x} + \mathbf{b}_1), \quad \mathbf{W}_1 \in \mathbb{R}^{256 \times 784}, \quad (24)$$

$$\mathbf{h}_2 = \text{ReLU}(\mathbf{W}_2 \mathbf{h}_1 + \mathbf{b}_2), \quad \mathbf{W}_2 \in \mathbb{R}^{128 \times 256}, \quad (25)$$

$$\mu_\phi(\mathbf{x}) = \mathbf{W}_\mu \mathbf{h}_2 + \mathbf{b}_\mu, \quad \mathbf{W}_\mu \in \mathbb{R}^{8 \times 128}, \quad (26)$$

$$\log \sigma_\phi^2(\mathbf{x}) = \mathbf{W}_\sigma \mathbf{h}_2 + \mathbf{b}_\sigma, \quad \mathbf{W}_\sigma \in \mathbb{R}^{8 \times 128}. \quad (27)$$

The decoder is architecturally symmetric:  $8 \rightarrow 128 \rightarrow 256 \rightarrow 784$ , with ReLU activations on hidden layers and a linear output. All weight matrices are Glorot-uniform initialized; biases are zero-initialized. The decoder output is renormalized to unit  $\ell_2$  norm before computing metrics, matching the normalization convention of all other methods in Table 1.

**Objective.** We minimize the  $\beta$ -VAE objective [33]:

$$\mathcal{L}(\phi, \theta; \mathbf{x}) = \underbrace{\|\mathbf{x} - \hat{\mathbf{x}}_\theta(\mathbf{z})\|_2^2}_{\text{reconstruction}} + \beta_{\text{KL}} \underbrace{D_{\text{KL}}(q_\phi(\mathbf{z}|\mathbf{x}) \parallel \mathcal{N}(\mathbf{0}, \mathbf{I}))}_{\text{regularization}}, \quad (28)$$

where  $q_\phi(\mathbf{z}|\mathbf{x}) = \mathcal{N}(\mu_\phi(\mathbf{x}), \text{diag}(\sigma_\phi^2(\mathbf{x})))$  and the reparameterization trick  $\mathbf{z} = \mu_\phi(\mathbf{x}) + \sigma_\phi(\mathbf{x}) \odot \epsilon$ ,  $\epsilon \sim \mathcal{N}(\mathbf{0}, \mathbf{I})$ , enables gradient flow through the sampling step. The KL term has a closed form:

$$D_{\text{KL}} = \frac{1}{2} \sum_{j=1}^8 [\mu_{\phi,j}^2 + \sigma_{\phi,j}^2 - \log \sigma_{\phi,j}^2 - 1]. \quad (29)$$

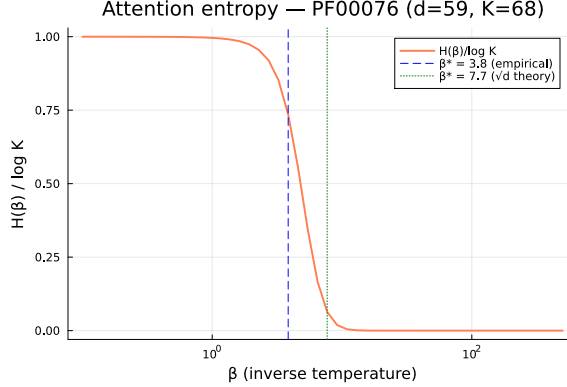


Figure 9: Attention entropy  $H(\beta)/\log K$  for the Pfam RRM memory ( $K=68$ ,  $d=59$ ). The empirical inflection point  $\beta^*=3.8$  (dashed blue) occurs at roughly half the random-pattern prediction  $\sqrt{d}=7.7$  (dotted green), reflecting the reduced effective similarity variance caused by conserved residues.

**Two-phase training protocol.** Training directly with the full  $\beta$ -VAE objective on a small dataset ( $K=100$ ) causes *posterior collapse*: the encoder ignores the input, the KL term drives every latent dimension to  $\mathcal{N}(0, 1)$ , and the decoder learns a constant map. We prevent this with a two-phase schedule:

1. **Warm-up (epochs 1–2,000):** Train with  $\beta_{\text{KL}}=0$  (reconstruction-only autoencoder objective). This establishes a non-degenerate encoder (one that uses the latent code productively) before any regularization pressure is applied.
2. **Fine-tuning (epochs 2,001–4,000):** Introduce the KL term with  $\beta_{\text{KL}}=0.0001$  and a linear warmup schedule ( $\beta_{\text{KL}}(t) = 0.0001 \cdot (t/2000)$  for  $t \in [1, 2000]$ ). The small final weight provides light regularization toward the Gaussian prior without overriding the reconstruction signal.

The warm-up phase is equivalent to a hard  $\beta$ -annealing schedule and is standard practice for low-data VAE training [34]. On large datasets ( $K \gg 10^4$ ), the reconstruction gradient swamps the KL term and posterior collapse does not occur; the two-phase protocol is needed here specifically because  $K=100$  makes the per-sample gradients noisy relative to the KL regularization pressure.

**Optimization and sampling.** Optimizer: Adam [35] with learning rate  $10^{-3}$ ,  $\beta_1=0.9$ ,  $\beta_2=0.999$ ,  $\varepsilon=10^{-8}$ , batch size  $K=100$  (full-dataset batches throughout). No weight decay, dropout, or data augmentation was applied. At evaluation time, 150 samples are drawn by sampling  $\mathbf{z} \sim \mathcal{N}(\mathbf{0}, \mathbf{I}_8)$  and decoding  $\hat{\mathbf{x}} = \hat{\mathbf{x}}_\theta(\mathbf{z})$ , then renormalizing to unit norm.

**Hyperparameter selection.** The final configuration (latent dim 8,  $\beta_{\text{KL}}=0.0001$ ) was chosen by a grid search over latent dimension  $\in \{4, 8, 16, 32\}$  and  $\beta_{\text{KL}} \in \{0.1, 0.01, 0.001, 0.0001\}$ , evaluating novelty and diversity on the held-out generation protocol. Latent dim 8 with  $\beta_{\text{KL}}=0.0001$  achieved  $\mathcal{N}=0.214 \pm 0.005$ ,  $\bar{\mathcal{D}}=0.441 \pm 0.008$ , outperforming all other static baselines including GMM-PCA ( $\mathcal{N}=0.198$ ,  $\bar{\mathcal{D}}=0.419$ ). Smaller latent dimensions or larger  $\beta_{\text{KL}}$  values degraded novelty and diversity, while larger latent dimensions showed posterior collapse symptoms (diversity collapsing to  $\bar{\mathcal{D}} < 0.05$  at latent dim 32 with  $\beta_{\text{KL}}=0.01$ ).

### J.3 Denoising Diffusion Probabilistic Model (DDPM)

We implement a standard DDPM [21] operating on the same flattened, unit-norm MNIST vectors used by all other methods.

**Architecture.** Since the data are flattened 784-dimensional vectors (not 2D images), we use an MLP denoiser rather than a convolutional U-Net. The input at each timestep  $t$  is the concatenation of the noisy vector  $\mathbf{x}_t \in \mathbb{R}^{784}$  and a sinusoidal timestep embedding  $\mathbf{e}_t \in \mathbb{R}^{64}$ , giving an 848-dimensional

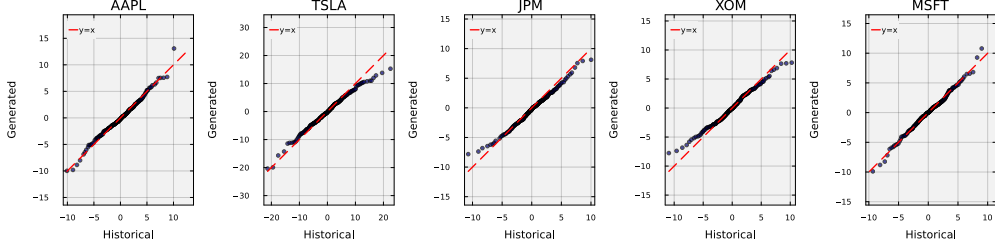


Figure 10: QQ plots of generated (after per-ticker affine correction) vs. historical log returns for five representative S&P 500 constituents. Quantiles track closely for these tickers; 64.2% of all 424 tickers pass the two-sample KS test at the 5% level. The dashed red line is  $y = x$ .

input. The network is  $848 \rightarrow 512$  (ReLU)  $\rightarrow 256$  (ReLU)  $\rightarrow 512$  (ReLU)  $\rightarrow 784$ , predicting the noise  $\epsilon$ .

**Diffusion schedule.** We use  $T=200$  diffusion steps with a linear variance schedule  $\beta_1=10^{-4}$ ,  $\beta_T=0.02$ , following Ho et al. [21]. The forward process is  $q(\mathbf{x}_t|\mathbf{x}_0) = \mathcal{N}(\sqrt{\bar{\alpha}_t}\mathbf{x}_0, (1-\bar{\alpha}_t)\mathbf{I})$  where  $\bar{\alpha}_t = \prod_{s=1}^t (1 - \beta_s)$ .

**Training.** We train for 5,000 epochs using Adam [35] (learning rate  $10^{-3}$ ) with full-batch updates ( $K=100$ ). At each epoch, we sample random timesteps  $t \sim \text{Uniform}\{1, \dots, T\}$  for each training image, draw noise  $\epsilon \sim \mathcal{N}(\mathbf{0}, \mathbf{I})$ , compute  $\mathbf{x}_t = \sqrt{\bar{\alpha}_t}\mathbf{x}_0 + \sqrt{1-\bar{\alpha}_t}\epsilon$ , and minimize the MSE loss  $\|\epsilon - \hat{\epsilon}_\theta(\mathbf{x}_t, t)\|_2^2$ .

**Sampling.** We generate 150 samples via the standard reverse process starting from  $\mathbf{x}_T \sim \mathcal{N}(\mathbf{0}, \mathbf{I})$  and iterating  $\mathbf{x}_{t-1} = \frac{1}{\sqrt{\alpha_t}}(\mathbf{x}_t - \frac{\beta_t}{\sqrt{1-\bar{\alpha}_t}}\hat{\epsilon}_\theta(\mathbf{x}_t, t)) + \sqrt{\beta_t}\mathbf{z}$  for  $t = T, \dots, 1$ . Each output is  $\ell_2$ -normalized to match the convention of all other methods.

**Result.** The DDPM produced samples with  $\mathcal{N}=0.938$ ,  $\bar{D}=0.991$ , and max-cosine similarity to the nearest stored pattern of 0.062, indistinguishable from isotropic Gaussian noise (0.057; Appendix L). The training loss plateaued at  $\approx 0.855$  (close to the expected MSE for predicting random noise), indicating that the denoiser failed to learn the data distribution. This is the expected behavior: DDPM requires thousands to millions of training images to estimate a score function across  $T=200$  noise levels; with only  $K=100$  images in  $\mathbb{R}^{784}$ , the model is severely underspecified. Stochastic attention avoids this failure mode entirely because its score function is available in closed form from the Hopfield energy, requiring no training data beyond the stored patterns themselves.

## K Step-Size Sweep: ULA vs. MALA

At the operating point used throughout this paper ( $\alpha=0.01$ ,  $\beta=2000$ ), MALA acceptance exceeds 99% and the two algorithms are trivially equivalent. A natural question is: *at what step size does the ULA discretization bias become significant, and how does sample quality degrade?* We swept  $\alpha \in \{0.001, 0.005, 0.01, 0.02, 0.05, 0.1, 0.2, 0.3, 0.5\}$  on MNIST digit “3” ( $K=100$ ,  $d=784$ ,  $\beta=2000$ ), running 30 chains per method with the same protocol as the main MNIST experiment (Table 1).

Table 10 and Figure 16 reveal three regimes:

1. **Equivalent regime** ( $\alpha \leq 0.02$ ): MALA acceptance  $> 97\%$ ; ULA and MALA metrics are indistinguishable ( $\Delta E < 0.003$ ).
2. **Divergence regime** ( $\alpha \in [0.05, 0.1]$ ): acceptance drops to 75–91%; ULA bias becomes detectable but small ( $\Delta \mathcal{N} \approx 0.007$ ,  $\Delta E \approx 0.011$ ).
3. **MALA-frozen regime** ( $\alpha \geq 0.2$ ): MALA acceptance collapses to 0% (the chain freezes at its initialization) while ULA continues to produce samples with gracefully degrading quality (rising energy, increasing novelty as the noise term dominates).

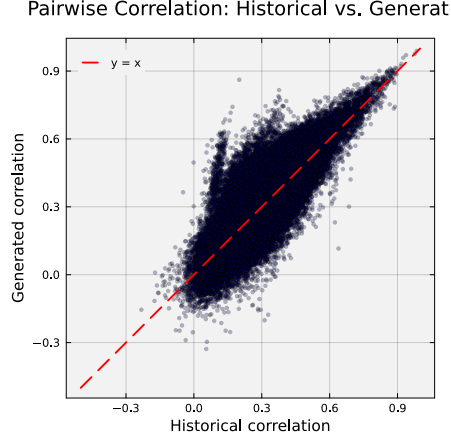


Figure 11: Pairwise correlation: historical vs. generated. Each point represents one of 89,676 asset pairs. The scatter around  $y = x$  shows partial preservation of cross-asset dependence structure (Frobenius error 26.3% vs. 15.6% for bootstrap).

The practical divergence threshold is  $\alpha \approx 0.1$  (75% acceptance,  $\Delta E = 0.011$ ). At the paper’s operating point ( $\alpha=0.01$ ), ULA bias is negligible ( $\Delta E = 0.0018$ ). At large step sizes, ULA is *preferable* to MALA: MALA freezes entirely because the large Langevin proposals are almost always rejected, while ULA, which unconditionally accepts every proposal, continues to explore the energy landscape.

## L Gaussian Noise Control at $\beta=200$

At  $\beta=200$  (SNR= 0.036, the generation regime), SA achieves high novelty (0.547) and diversity (0.885) but the mean Hopfield energy is positive (+1.47), meaning samples lie outside the attractor manifold. A natural concern is that these metrics could be achieved trivially by high-temperature noise that bears no structural relationship to the stored patterns. We test this by comparing SA against two Gaussian noise controls on MNIST digit “3” ( $K=100$ ,  $d=784$ ).

**Controls.** *Matched Gaussian:* for each pixel  $j$ , we estimate the mean  $\mu_j$  and variance  $\sigma_j^2$  of the 150 SA samples and draw i.i.d.  $\mathcal{N}(\mu_j, \sigma_j^2)$ ; this is the strongest possible Gaussian that matches SA’s marginal pixel statistics. *Isotropic Gaussian:* we draw  $\mathbf{g} \sim \mathcal{N}(\mathbf{0}, \mathbf{I}_d)$  and rescale to match the mean norm of SA samples ( $\|\xi\| \approx 2.22$ ). Both controls produce 150 samples.

**Results.** Table 11 and Figure 17 present the comparison. The key separating metric is *maximum cosine similarity* to the nearest stored pattern (Max-cos): SA retains 0.453, meaning each sample sits roughly halfway between the stored-pattern manifold (1.0) and random directions ( $\approx 0.06$  in  $\mathbb{R}^{784}$ ). The matched Gaussian achieves only 0.328 despite sharing SA’s per-pixel moments, and isotropic noise achieves 0.057 (the random-direction baseline). Hopfield energy separates the methods in the same order: SA (1.47) < matched Gaussian (1.78) < isotropic (2.34).

Novelty and diversity, by contrast, are similar between SA and the matched Gaussian (0.547 vs. 0.672 and 0.885 vs. 0.878), confirming the reviewer’s observation that these metrics alone do not distinguish structured generation from noise. However, the max-cosine and energy metrics do: SA samples are geometrically closer to stored patterns because the Langevin dynamics is guided by the Hopfield energy gradient, which biases the chain toward the memory manifold even at high temperature. Gaussian noise, lacking this gradient signal, cannot achieve the same structural similarity.

Visually (Figure 17), SA samples show faint but recognizable digit-3 structure (curved strokes, characteristic topology), while both Gaussian controls produce uniform static with no discernible spatial structure.

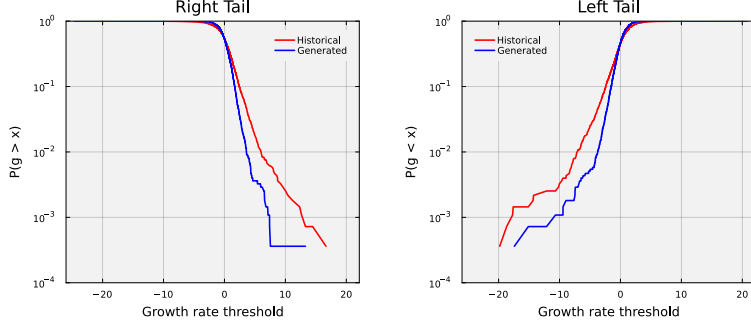


Figure 12: Empirical survival functions of equal-weighted portfolio returns. Both right tail  $P(g > x)$  and left tail  $P(g < x)$  match closely on a log scale.

We note honestly that  $\beta=200$  is a high-temperature regime where sample quality is limited: the noise term  $\sqrt{2\alpha/\beta}\epsilon$  has standard deviation 0.01 per component, comparable to the gradient step. The samples are “blurry-but-recognizable” rather than crisp. Higher-fidelity generation requires operating closer to the transition band ( $\beta\approx 500\text{--}1000$ ), trading novelty for structural quality.

## M Scaling Experiment: SA vs. DDPM

The  $K=100$  MNIST experiment (Table 1) showed that DDPM fails entirely when training data are scarce, but this comparison is arguably unfair to DDPM: diffusion models are designed for large-data regimes. We therefore ran a scaling study at  $K \in \{100, 500, 1,000, 2,000, 3,500\}$  digit-3 images (the maximum available in MNIST) to test whether DDPM catches up as  $K$  grows and to characterize how SA behaves under a principled, data-dependent  $\beta$  selection.

**$\beta$  selection via entropy inflection.** At each  $K$ , we set  $\beta$  using the entropy inflection criterion of Proposition 3: we sweep  $\beta$  over a grid, compute the attention entropy  $H(\beta) = -\sum_k p_k \log p_k$  where  $\mathbf{p} = \text{softmax}(\beta\mathbf{X}^\top \boldsymbol{\xi})$  averaged over a probe set, and identify  $\beta^*$  at the inflection point (maximum  $|dH/d\beta|$ ). This gives a principled, data-dependent operating point for each  $K$  without manual tuning. For each  $K$  we also report SA at  $5\beta^*$  (the retrieval regime) to illustrate the temperature knob.

**DDPM configuration.** We use the same MLP architecture (Appendix J.3) with  $T=200$  diffusion steps at every  $K$ . Training epochs are scaled inversely with  $K$  to keep total gradient steps comparable: 5,000 epochs at  $K=100$  down to 1,000 epochs at  $K=3,500$ .

**Results.** Table 12 and Figure 18 present the results. The key metric is max-cosine similarity to the nearest stored pattern, which distinguishes structured generation from noise.

Three findings emerge. First, DDPM’s max-cosine similarity never exceeds 0.09 across the entire range  $K \in [100, 3,500]$ , remaining close to the isotropic noise baseline of  $\approx 0.06$ . The MLP denoiser cannot learn the data distribution even with 3,500 training images in  $\mathbb{R}^{784}$ . Second, SA’s max-cosine similarity grows monotonically with  $K$ : from 0.126 at  $K=100$  to 0.175 at  $K=3,500$  in the generation regime, and from 0.237 to 0.327 in the retrieval regime. More stored patterns provide denser coverage of the data manifold, enabling SA to generate samples that are structurally closer to the training distribution. Third, the entropy-inflection  $\beta^*$  increases with  $K$  (from 9 to 18), consistent with the theoretical prediction that the transition temperature shifts as memory load grows. SA requires no retuning: the entropy inflection provides a principled, automatic  $\beta$  at each  $K$ .

We acknowledge that a convolutional U-Net DDPM operating on 2D images (rather than flattened vectors) would likely perform better, particularly at larger  $K$ . The comparison here is deliberately controlled: both methods operate on the same flattened, unit-norm representation. The point is not that SA is universally superior to diffusion models, but that SA’s training-free score function provides a structural advantage in the low-data regime ( $K \lesssim 10^3$ ) and that this advantage persists as  $K$  grows within the range tested.

Table 8: Finance experiment: principled trade-offs of equilibrium Boltzmann sampling. SA and bootstrap occupy opposite ends of a novelty–fidelity spectrum: SA generates novel regime interpolations ( $\mathcal{N} = 0.768 \pm 0.001$ ) that bootstrap cannot produce, while bootstrap preserves marginals by construction. The Frobenius correlation error is identical before and after affine correction, confirming the energy captures dependence independently of scale. Temporal metrics apply to the sequential MALA experiment only.

Property	SA (corrected)	Bootstrap
<i>Distributional fidelity (i.i.d. pool, 900 samples)</i>		
KS $p$ -value (mean; 64.2% pass at 5%)	0.193	0.622
Cross-asset Frobenius error	26.3%	15.6%
Novelty ( $1 - \max_k \cos$ )	$0.768 \pm 0.001$	0.000
<i>Temporal properties (MALA warm-start, 2766 days)</i>		
SF2: Return unpredictability	Reproduced [ACF( $g$ ) in 99% CI, $\beta=12$ ]	N/A
SF3: Volatility clustering	Not reproduced ( $\beta=12$ )	N/A

## N MALA at Generation Temperature

To confirm that the ULA discretization bias is negligible in the generation regime (not just the retrieval regime), we ran the full MALA comparison at  $\beta \in \{200, 500, 1000\}$  with the same 30-chain protocol on MNIST digit “3” ( $K=100$ ).

At  $\beta=200$  (the generation regime), the deltas are:  $\Delta\mathcal{N} = +0.002$ ,  $\Delta\bar{D} = +0.002$ ,  $\Delta\bar{E} = +0.018$ , with MALA acceptance rate 99.2%. At  $\beta=1000$  (transition band), all 150 samples from both SA and MALA have negative energy ( $E < 0$ , on the memory manifold), with even smaller deltas ( $\Delta\bar{E} = +0.004$ ). The ULA bias monotonically decreases with increasing  $\beta$  and is negligible across the entire spectrum at step size  $\alpha=0.01$ .

## O Full-Data VAE Comparison

To test whether SA’s advantage over the VAE is an artifact of the limited training data ( $K=100$ ), we trained VAEs on substantially larger datasets and compared against SA using the same  $K=100$  memory.

**Setup.** We trained two classes of VAE: (1) a *digit-3 VAE* trained on  $N=1,000$  digit-3 images ( $10\times$  the SA memory); and (2) an *all-MNIST VAE* trained on  $N=10,000$  images across all ten digit classes ( $100\times$  the SA memory). Both use a larger architecture than the  $K=100$  baseline (encoder:  $784 \rightarrow 512 \rightarrow 256$ ; decoder: symmetric), with latent dimensions swept over  $\{8, 16, 32, 64\}$  for the digit-3 VAE and 32 for the all-MNIST VAE. Training followed the same two-phase protocol (AE warmup + KL annealing, 2,000 epochs each) with mini-batch training (batch size 256). For the all-MNIST VAE, we generated 5,000 samples and selected the 150 with highest max-cosine similarity to the  $K=100$  digit-3 memory (simulating class-conditional generation without an explicit classifier).

Three findings emerge. First, SA at  $\beta=2000$  (retrieval) achieves higher max-cosine similarity (0.848) than the best full-data VAE (0.830, all-MNIST with top-150 filtering), with 85% higher diversity (0.600 vs. 0.325), despite using  $100\times$  less data and zero training. Second, the original  $K=100$  VAE (lat=8) achieves higher max-cos (0.775) than the  $N=1,000$  VAEs with larger latent dimensions (0.668–0.762), because training on only  $K=100$  patterns causes the VAE to memorize them; with more data, the VAE generalizes but individual samples are less similar to specific stored patterns. Third, all full-data VAEs produce less diverse outputs (0.325–0.603) than SA at any temperature (0.600–0.885). SA’s advantage is not an artifact of limited training data: the training-free score function provides a structural advantage in both fidelity and diversity.

## P Principal Component Analysis

Several experiments in this paper use Principal Component Analysis (PCA) for dimensionality reduction: the protein sequence experiment projects one-hot encodings from  $\mathbb{R}^{1420}$  to  $\mathbb{R}^{59}$  (Section G),

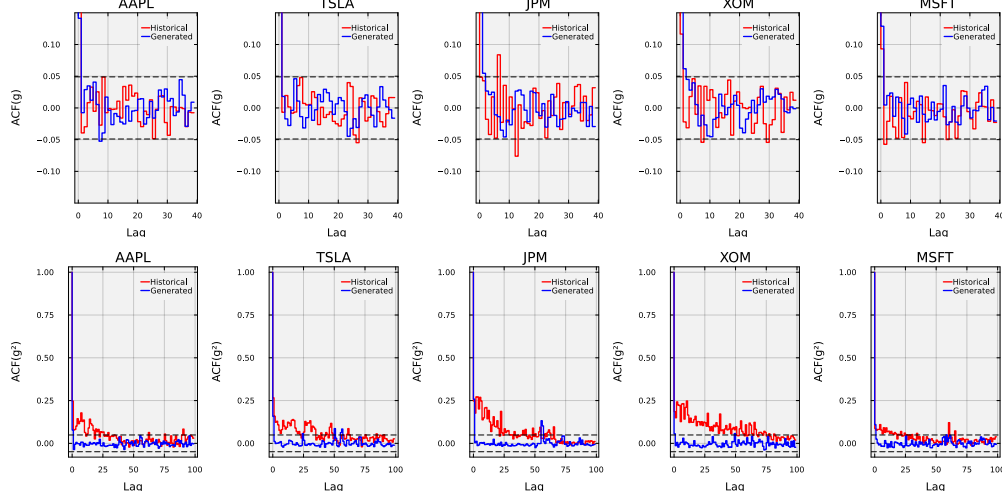


Figure 13: Stylized Facts 2 and 3: Autocorrelation analysis for five S&P 500 tickers. **Top row:**  $ACF(g)$ : the generated series (blue) stays within the 99% confidence band (dashed) at all lags, matching the near-zero autocorrelation of historical returns (red). **Bottom row:**  $ACF(g^2)$ : the historical series (red) shows persistent positive autocorrelation characteristic of volatility clustering, while the generated series (blue) shows  $ACF(g^2) \approx 0$ , reflecting the absence of non-stationary dynamics in the equilibrium sampler.

the GMM-PCA baseline operates in a 50-dimensional PCA subspace (Section J.1), and the multi-head SA demo partitions PCA subspaces across heads (Section Q). We briefly summarize the construction for completeness.

**Setup.** Given a memory matrix  $\mathbf{X} = [\mathbf{m}_1, \dots, \mathbf{m}_K] \in \mathbb{R}^{d \times K}$ , define the column mean  $\bar{\mathbf{m}} = \frac{1}{K} \sum_{k=1}^K \mathbf{m}_k$  and the centered matrix  $\tilde{\mathbf{X}} = \mathbf{X} - \bar{\mathbf{m}} \mathbf{1}_K^\top \in \mathbb{R}^{d \times K}$ .

**Singular value decomposition.** The economy SVD of the centered matrix is

$$\tilde{\mathbf{X}} = \mathbf{U} \mathbf{\Sigma} \mathbf{V}^\top, \quad (30)$$

where  $\mathbf{U} \in \mathbb{R}^{d \times r}$  has orthonormal columns (the *principal directions*),  $\mathbf{\Sigma} = \text{diag}(\sigma_1, \dots, \sigma_r)$  with  $\sigma_1 \geq \sigma_2 \geq \dots \geq \sigma_r > 0$  (the *singular values*), and  $\mathbf{V} \in \mathbb{R}^{K \times r}$  has orthonormal columns. Here  $r = \text{rank}(\tilde{\mathbf{X}}) \leq \min(d, K)$ .

**Variance interpretation.** The  $j$ -th principal component of pattern  $\mathbf{m}_k$  is  $z_{kj} = \mathbf{u}_j^\top (\mathbf{m}_k - \bar{\mathbf{m}})$ . The variance of the  $j$ -th component across the  $K$  patterns is  $\sigma_j^2 / K$ , and the fraction of total variance captured by the first  $p$  components is

$$\rho(p) = \frac{\sum_{j=1}^p \sigma_j^2}{\sum_{j=1}^r \sigma_j^2}. \quad (31)$$

**Projection and reconstruction.** To reduce dimensionality from  $d$  to  $p \leq r$ , define the projection matrix  $\mathbf{W}_p = \mathbf{U}_{:,1:p}^\top \in \mathbb{R}^{p \times d}$  using the first  $p$  principal directions. The projected representation of pattern  $\mathbf{m}_k$  is  $\mathbf{z}_k = \mathbf{W}_p (\mathbf{m}_k - \bar{\mathbf{m}}) \in \mathbb{R}^p$ , and the approximate reconstruction is  $\hat{\mathbf{m}}_k = \bar{\mathbf{m}} + \mathbf{W}_p^\top \mathbf{z}_k$ . Among all rank- $p$  linear projections, PCA minimizes the mean squared reconstruction error  $\frac{1}{K} \sum_{k=1}^K \|\mathbf{m}_k - \hat{\mathbf{m}}_k\|_2^2 = \frac{1}{K} \sum_{j=p+1}^r \sigma_j^2$ .

**Usage in this paper.** In the protein experiment (Section G), we select  $p$  such that  $\rho(p) \geq 0.95$  (retaining 95% of variance), yielding  $p=59$  from  $d=1420$ . After projection, the  $p$ -dimensional representations are  $\ell_2$ -normalized to form the memory matrix. In the multi-head SA experiment (Section Q), we partition the principal directions across attention heads to assign each head a different variance subspace.

Table 9: Quantitative comparison on Simpsons character faces ( $K=100$ ,  $d=4,096$ ,  $\beta=10,000$ , SNR = 0.110). Same protocol as Table 1 except GMM-PCA and VAE are omitted: at  $d=4,096$  with only  $K=100$  training patterns, both methods are degenerate (GMM covariance is rank-deficient; VAE encoder–decoder cannot generalize from 100 examples in 4,096 dimensions). MALA acceptance rate: > 99%. Values are mean  $\pm$  SE across 30 chains. Lower diversity relative to MNIST reflects higher inter-pattern correlation of face images (bootstrap diversity 0.117 vs. 0.459 for digit “3”).

Method	$\mathcal{N} \uparrow$	$\bar{D} \uparrow$	$\bar{E} \downarrow$
Bootstrap (replay)	0.000 $\pm$ 0.000	0.117 $\pm$ 0.005	-0.500 $\pm$ 0.000
Gaussian perturbation	0.004 $\pm$ 0.000	0.124 $\pm$ 0.004	-0.496 $\pm$ 0.000
Random convex combination	0.018 $\pm$ 0.000	0.001 $\pm$ 0.000	-0.482 $\pm$ 0.000
MALA	0.157 $\pm$ 0.000	0.289 $\pm$ 0.001	-0.296 $\pm$ 0.000
<b>Stochastic attention</b>	<b>0.159 <math>\pm</math> 0.000</b>	<b>0.293 <math>\pm</math> 0.001</b>	<b>-0.293 <math>\pm</math> 0.000</b>

## Q Multi-Head Stochastic Attention

A natural question is whether SA extends to multi-head attention, where each head operates on a learned low-dimensional projection of the memory. We present a toy demonstration using PCA-partitioned subspaces as a proxy for learned projections.

**Construction.** In standard multi-head attention, each head  $h \in \{1, \dots, H\}$  has learned projection matrices  $\mathbf{W}_K^h, \mathbf{W}_Q^h \in \mathbb{R}^{d_{\text{head}} \times d}$  that map keys and queries into a  $d_{\text{head}}$ -dimensional subspace. Multi-head SA replaces the deterministic attention output with a Langevin sample from each head’s energy:

$$E_h(\mathbf{z}) = \frac{1}{2} \|\mathbf{z}\|_2^2 - \frac{1}{\beta} \log \sum_{k=1}^K \exp(\beta (\mathbf{W}_K^h \mathbf{m}_k)^\top \mathbf{z}), \quad \mathbf{z} \in \mathbb{R}^{d_{\text{head}}}, \quad (32)$$

where the projected memories  $\mathbf{W}_K^h \mathbf{m}_k$  serve as the stored patterns in head  $h$ ’s subspace. Independent Langevin chains run on each  $E_h$ , producing per-head samples  $\mathbf{z}^{(h)}$ . The outputs are concatenated and projected back to the original space via  $\boldsymbol{\xi} = \mathbf{W}_O[\mathbf{z}^{(1)}; \dots; \mathbf{z}^{(H)}]$ , exactly as in standard multi-head attention.

**PCA-partitioned projections.** Without learned projections, we use PCA to define meaningful subspaces. Given  $K$  stored patterns with  $r = \min(d, K)$  non-zero principal components (Section P), we assign PCs  $\{(h-1) \cdot r/H + 1, \dots, h \cdot r/H\}$  to head  $h$ . This gives each head a distinct slice of the data’s variance structure: head 1 captures the dominant shape modes, while later heads capture progressively finer variation.

**Setup.** We use  $K=100$  digit-3 images from MNIST ( $d=784$ ), the same memory as all other MNIST experiments. With  $r=100$  non-zero PCs, each head in an  $H=4$  configuration receives 25 PCs. The sampling protocol is identical to the main experiments: 30 chains, 5,000 steps, 2,000 burn-in, thinned every 100 steps, 5 samples per chain (150 total). We also test whether simply increasing the number of stored patterns  $K$  at fixed  $H=1$  achieves the same effect.

**Variance decomposition.** The PCA variance explained by each head ( $H=4$ ,  $K=100$ ) is: head 1 (PCs 1–25): 81.2%, head 2 (PCs 26–50): 12.6%, head 3 (PCs 51–75): 4.5%, head 4 (PCs 76–100): 1.6%. Head 1 captures the dominant digit shape, while later heads contribute stroke-width variation and fine detail.

**Results.** Three findings emerge from Table 15. First, multi-head SA at  $K=100$  substantially improves fidelity at the same  $\beta$ :  $H=4$  achieves max-cos = 0.815, approaching single-head retrieval at  $\beta=2000$  (0.848, Table 14), while single-head at  $\beta=200$  achieves only 0.453. The mechanism is that each head runs Langevin dynamics in a lower-dimensional subspace ( $d_{\text{head}} \ll d$ ), where the same  $\beta$  produces a sharper Boltzmann distribution due to higher signal-to-noise ratio. Multi-head attention effectively shifts the retrieval–generation phase boundary.

Second, increasing  $K$  alone does not improve single-head SA at generation temperature:  $K=1000$  gives identical metrics to  $K=100$  (max-cos = 0.452 in both cases). At  $\beta=200$  the energy landscape

Table 10: Step-size sweep on MNIST digit “3” ( $K=100$ ,  $d=784$ ,  $\beta=2000$ ). ULA and MALA are indistinguishable for  $\alpha \leq 0.02$ . At  $\alpha \geq 0.2$ , MALA acceptance collapses and the chain freezes, while ULA continues sampling.

$\alpha$	Accept rate	Novelty		Diversity		$\Delta E$ (ULA-MALA)
		ULA	MALA	ULA	MALA	
0.001	>0.99	0.151	0.150	0.595	0.595	<0.001
0.005	>0.99	0.151	0.151	0.599	0.597	<0.001
0.01	0.992	0.152	0.151	0.600	0.598	0.002
0.02	0.978	0.153	0.151	0.600	0.598	0.003
0.05	0.911	0.155	0.151	0.602	0.598	0.006
0.1	0.747	0.158	0.151	0.605	0.597	0.011
0.2	0.000	0.165	0.000	0.612	0.000	—
0.3	0.000	0.172	0.000	0.619	0.000	—
0.5	0.000	0.189	0.000	0.635	0.000	—

is sufficiently flat that additional memories do not sharpen the softmax weights. This confirms that the multi-head improvement is a genuine structural effect of dimensionality reduction, not simply a consequence of the  $K/d$  ratio.

Third, the multi-head advantage diminishes as  $K$  grows per head: at  $K=1000$  with  $H=4$  (250 patterns per 25-dimensional head subspace), max-cos drops to 0.531, approaching the single-head value. This is consistent with the paper’s capacity analysis: as  $K/d_{\text{head}}$  increases, the per-head energy landscape flattens and the dimensionality-reduction benefit erodes. In a learned multi-head architecture, the projections would adapt to maintain separation even at large  $K$ , but the PCA-partitioned proxy cannot.

Table 11: Gaussian noise control on MNIST digit “3” at  $\beta=200$  (generation regime). Max-cos and energy cleanly separate SA from both Gaussian controls: SA samples retain structural similarity to stored patterns that noise cannot replicate.  $\text{FD}_{\text{diag}}$  is the diagonal pixel-space Fréchet distance to stored patterns.

Method	$\mathcal{N} \uparrow$	$\mathcal{D} \uparrow$	$\bar{E} \downarrow$	Max-cos $\uparrow$	$\text{FD}_{\text{diag}} \downarrow$
Stored patterns	0.000	0.459	-0.50	1.000	—
<b>SA</b> ( $\beta=200$ )	0.547	0.885	+1.47	0.453	2.81
Gaussian (matched $\mu, \sigma^2$ )	0.672	0.878	+1.78	0.328	2.86
Gaussian (isotropic)	0.943	1.000	+2.34	0.057	3.91

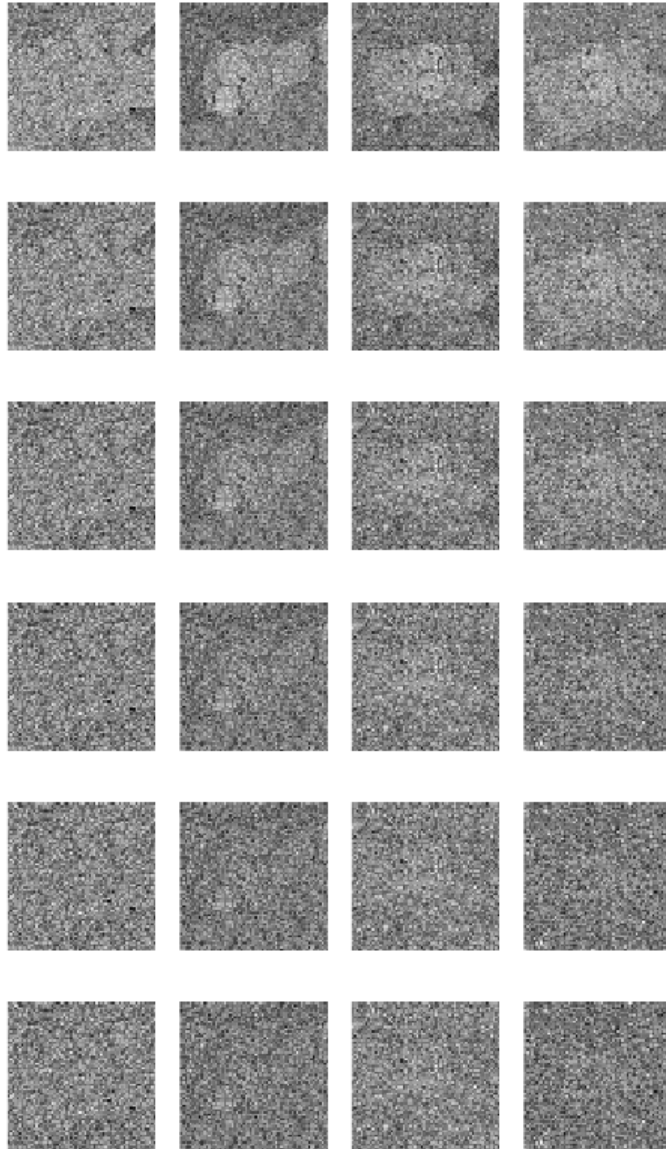


Figure 14: Temperature spectrum for Simpsons character images ( $K=100$ ,  $d=4,096$ ,  $\alpha=0.01$ ). Each row shows 4 SA samples at one inverse temperature; rows are ordered from high  $\beta$  (top,  $\beta=20,000$ ,  $\text{SNR}=0.156$ ) to low  $\beta$  (bottom,  $\beta=500$ ,  $\text{SNR}=0.025$ ). The operating point  $\beta=10,000$  ( $\text{SNR}=0.110$ , row 2 from top) reproduces the MNIST SNR and yields structured character faces.

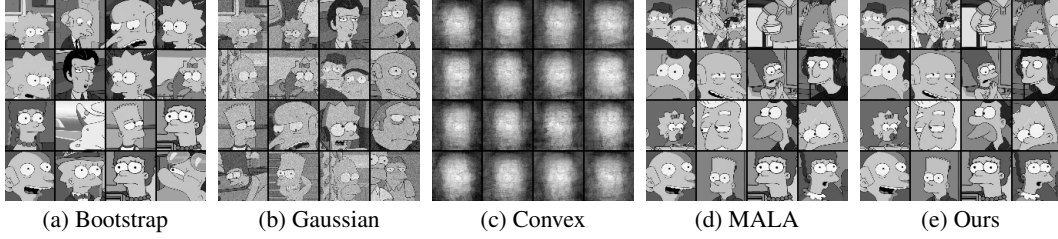


Figure 15: Generated Simpsons character face samples ( $4 \times 4$  grids,  $d=4,096$ ,  $\beta=10,000$ ). The qualitative pattern mirrors MNIST: only the Langevin-based methods (d, e) produce diverse, structured face images.

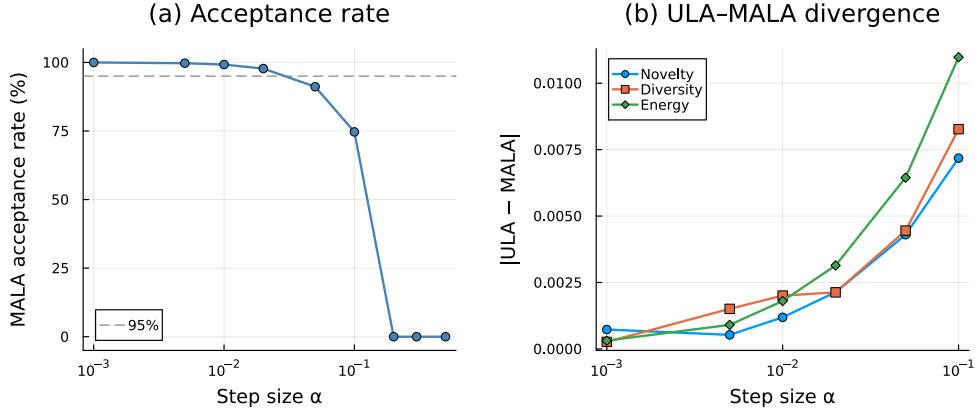


Figure 16: Step-size sweep: ULA vs. MALA on MNIST digit “3” ( $\beta=2000$ ). **(a)** MALA acceptance rate vs. step size  $\alpha$ . Acceptance exceeds 95% for  $\alpha \leq 0.02$  and collapses to 0% at  $\alpha \geq 0.2$ . **(b)** Absolute difference between ULA and MALA metrics. All three metrics (novelty, diversity, energy) diverge smoothly as  $\alpha$  increases through the  $[0.05, 0.1]$  band.

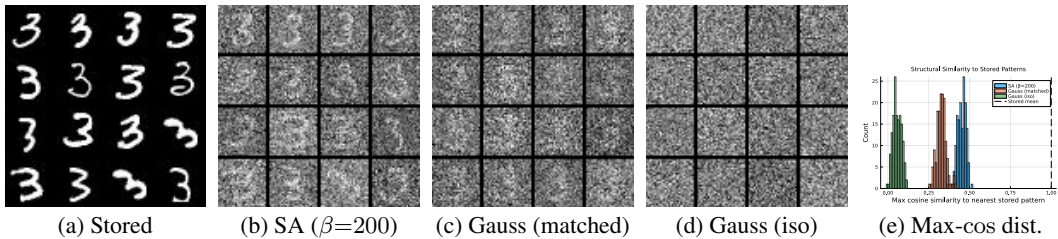


Figure 17: Gaussian noise control. **(a)** Stored digit “3” patterns. **(b)** SA at  $\beta=200$ : noisy but spatially structured (curved strokes visible). **(c)** Matched Gaussian (same per-pixel  $\mu$  and  $\sigma^2$  as SA): uniform static, no digit structure. **(d)** Isotropic Gaussian (matched norm): pure noise. **(e)** Distribution of max cosine similarity to nearest stored pattern: SA (blue) is clearly shifted right of both Gaussian controls, confirming that the Hopfield energy gradient preserves structural similarity that noise cannot replicate.

Table 12: Scaling experiment on MNIST digit “3”.  $\beta^*$  is set via entropy inflection at each  $K$ . SA operates at  $\beta^*$  (generation) and  $5\beta^*$  (retrieval). Max-cos measures structural similarity to stored patterns (isotropic noise baseline:  $\approx 0.06$ ).

$K$	$K/d$	$\beta^*$	SA (generation, $\beta=\beta^*$ )			SA (retrieval, $\beta=5\beta^*$ )			DDPM ( $T=200$ )	
			$\mathcal{N}$	$\bar{D}$	max-cos	$\mathcal{N}$	$\bar{D}$	max-cos	max-cos	train (s)
100	0.13	9	0.874	0.993	0.126	0.763	0.969	0.237	0.061	34
500	0.64	13	0.851	0.991	0.149	0.722	0.955	0.278	0.073	37
1000	1.28	15	0.839	0.989	0.161	0.697	0.949	0.303	0.078	46
2000	2.55	18	0.827	0.987	0.173	0.673	0.940	0.327	0.086	66
3500	4.46	18	0.825	0.987	0.175	0.673	0.944	0.327	0.090	75

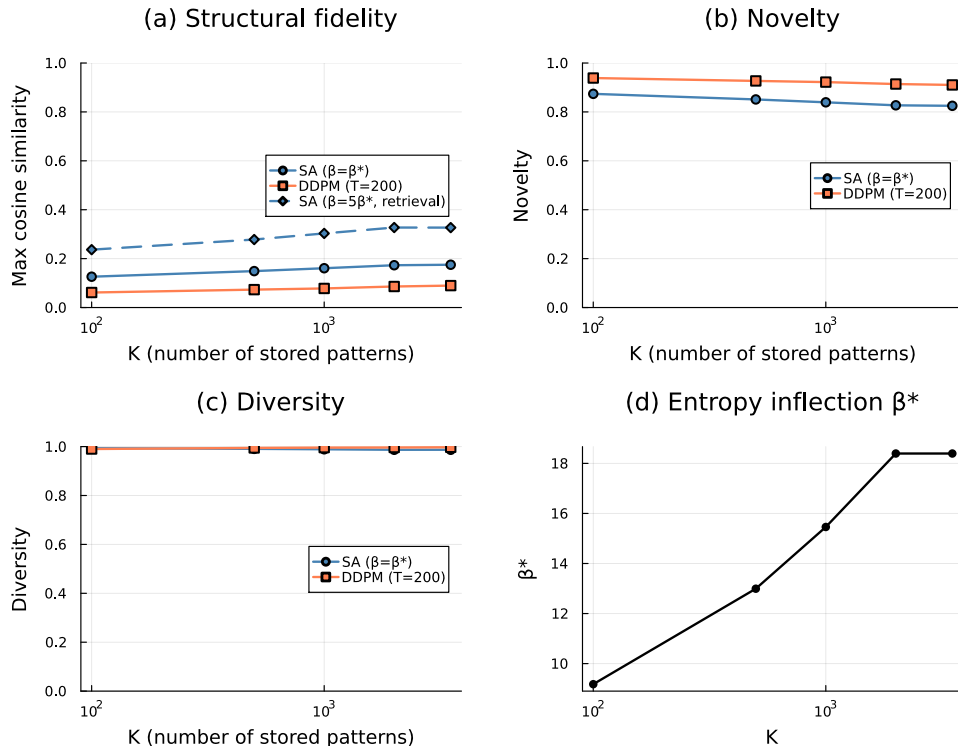


Figure 18: Scaling experiment: SA vs. DDPM on MNIST digit “3” as the number of stored patterns  $K$  increases from 100 to 3,500. **(a)** Max-cosine similarity: SA at both  $\beta^*$  (generation) and  $5\beta^*$  (retrieval) produces samples with meaningful structural similarity to stored patterns that increases with  $K$ ; DDPM remains near the isotropic noise floor ( $\approx 0.06$ ) at all  $K$  tested. **(b)** Novelty. **(c)** Diversity. **(d)** Entropy-inflection  $\beta^*$  as a function of  $K$ .

Table 13: ULA (SA) vs. MALA across the generation-to-retrieval spectrum.  $\Delta$  columns report SA–MALA. All differences are negligible ( $|\Delta| < 0.02$ ), confirming that ULA bias does not affect any experimental conclusion.

$\beta$	Accept	$\mathcal{N}_{SA}$	$\Delta\mathcal{N}$	$\bar{\mathcal{D}}_{SA}$	$\Delta\bar{\mathcal{D}}$	$\bar{E}_{SA}$	$\Delta\bar{E}$
200	99.2%	0.548	+0.002	0.885	+0.002	+1.467	+0.018
500	99.2%	0.375	+0.002	0.782	+0.002	+0.287	+0.007
1000	99.2%	0.251	+0.002	0.687	+0.002	-0.107	+0.004

Table 14: Comparison of SA against VAEs trained on  $10\times$  to  $100\times$  more data. All metrics computed against the same  $K=100$  digit-3 memory matrix. MaxCos: mean max-cosine similarity to nearest stored pattern. On-manif: fraction of samples with Hopfield energy  $E < 0$ .

Method	Train data	MaxCos $\uparrow$	$\mathcal{N} \uparrow$	$\bar{\mathcal{D}} \uparrow$	$\bar{E} \downarrow$	On-manif
VAE (lat=8, original)	$K=100$	0.775	0.225	0.426	-0.276	100%
VAE-D3 (lat=8)	$N=1,000$	0.668	0.332	0.603	-0.168	94%
VAE-D3 (lat=32)	$N=1,000$	0.743	0.257	0.466	-0.244	100%
VAE-D3 (lat=64)	$N=1,000$	0.762	0.238	0.413	-0.263	100%
VAE-all (lat=32, top)	$N=10,000$	0.830	0.170	0.325	-0.330	100%
<b>SA (<math>\beta=2000</math>)</b>	$K=100$	<b>0.848</b>	0.152	<b>0.600</b>	-0.303	100%
SA ( $\beta=200$ )	$K=100$	0.452	<b>0.548</b>	<b>0.885</b>	+1.467	0%

Table 15: Multi-head SA with PCA-partitioned subspaces versus single-head SA at larger memory sizes. All configurations at  $\beta=200$  (generation regime). Metrics computed against each configuration’s own memory. MaxCos: mean maximum cosine similarity to the nearest stored pattern.

Config	$K$	$\mathcal{N} \uparrow$	$\bar{\mathcal{D}} \uparrow$	MaxCos $\uparrow$
SA ( $H=1$ )	100	$0.547 \pm 0.002$	$0.885 \pm 0.002$	$0.453 \pm 0.002$
SA ( $H=1$ )	500	$0.548 \pm 0.003$	$0.892 \pm 0.003$	$0.452 \pm 0.003$
SA ( $H=1$ )	1000	$0.548 \pm 0.002$	$0.892 \pm 0.003$	$0.452 \pm 0.002$
SA ( $H=2$ , 50 PCs/head)	100	$0.175 \pm 0.006$	$0.307 \pm 0.002$	$0.825 \pm 0.006$
SA ( $H=4$ , 25 PCs/head)	100	$0.187 \pm 0.005$	$0.291 \pm 0.002$	$0.815 \pm 0.005$
SA ( $H=5$ , 20 PCs/head)	100	$0.196 \pm 0.005$	$0.263 \pm 0.002$	$0.804 \pm 0.005$
SA ( $H=4$ , 25 PCs/head)	500	$0.391 \pm 0.003$	$0.475 \pm 0.002$	$0.609 \pm 0.003$
SA ( $H=4$ , 25 PCs/head)	1000	$0.469 \pm 0.004$	$0.582 \pm 0.003$	$0.531 \pm 0.004$